Chapter 4 : Results and Discussion

This chapter is devoted to analyse the as-received materials (CP-Ti (grade-2 titanium) and Ti-6Al-4V) used during the study and develop the method for dissimilar welding of these alloys and the characterization of the prepared weld. The pulsed GTAW process was utilised for welding during the study and was also compared with the weld prepared using conventional GTAW. All the welds were prepared using an indigenously developed shielding setup, which helped protect the weldment from atmospheric contamination.

The current study is divided into four parts, and each part is dedicated to solve the objectives of the research work. In the first part of the study, the effect of current pulsing was observed with the help of BOP welding on a Ti-6Al-4V alloy sheet. In the second part of the study, the effect of electrode tip angle was analysed on various geometrical parameters with the help of BOP welding on CP-Ti sheet using different electrode tip angles. In the third part of the study, several BOP welding trials were performed at various steps of pulse parameters to observe the effect of each parameter and select the pulse parameters for maximum penetration at minimum heat input. In the fourth part of the study, the welding of dissimilar titanium alloys was carried out at optimised pulsed parameters and varying frequencies. The welds prepared during the study were analysed using optical, structural, elemental, and mechanical testing.

4.1 Effect of current pulsing during GTAW on Ti-6Al-4V weld

After looking at the key challenges during the welding of titanium alloys, like atmospheric contamination and severe grain growth in the weld and HAZ region.

The atmospheric contamination during the welding of titanium alloys can be avoided using shielding setup (refer to section 3.6). But the problem of severe grain coarsening in the weld and HAZ, formation of long axial grains during conventional-GTAW is still persisting (refer to Figure 3.13 (a)). To avoid the problem of grain coarsening and long axial grains the current pulsing was utilized during welding. The BOP welding was prepared using the conventional and pulsed current GTAW process by adjusting the parameters in such a way that the same heat input was supplied in both types of welds. Current pulsing during welding helped in avoiding the long axial grain (refer to Figure 3.13 (b)). Current pulsing in GTAW causes periodic heating and cooling, inducing thermal gradients that promote faster cooling during low-current phases. This rapid cooling restricts grain growth, producing a finer microstructure by limiting diffusion and recrystallization. Finer grains increase grain boundary area, acting as barriers to dislocation motion, thus raising the material's hardness. Additionally, controlled heat input minimizes the heat-affected zone, preventing excessive grain coarsening and maintaining improved microhardness in the weld region. The effect of current pulsing during GTAW on microstructural and microhardness changes was analysed and compared with conventional GTAW.

Cleaned coupons of 100 mm×50 mm and 2 mm thick Ti-6Al-4V (α+β alloy) were taken for the experimentation. The chemical composition (wt.%) of as-received Ti-6Al-4V is listed in Table 3.1. The Lincoln Aspect 300 AC/DC TIG welding machine assembled with a servo-controlled trolley and shielding setup was used for BOP welding. The complete list of welding parameters for conventional and pulsed GTAW are mentioned in Table 3.5 and Table 3.6. Obtained atmospheric contamination free weld beads were cross-sectionally cut, and samples for metallographic study and microhardness measurement were extracted. Prepared

metallographic samples were etched and utilized for microstructural assessment and microhardness measurement. Microstructure of different regions was captured using an optical microscope and microhardness was measured using a semiautomatic microhardness tester. Vickers hardness numbers (VHN) were recorded using a diamond pyramidal indenter under a load of 200 g for a dwell time of 10 seconds.

4.1.1 Bead on plate welding

Radiographic quality BOP welding was performed on the Ti-6Al-4V alloy using the conventional and pulsed GTAW processes, and a comparison between both has been drawn in Section 3.7.2. Majorly, current pulsing during GTAW helps in avoiding the formation of large axial grains at the center of the welds and helps in forming discrete solidification marks, sometime also known as ripples. BOP welding prepared using conventional and pulsed GTAW is shown in Figure 3.2 (a-b).

4.1.2 Microstructural analysis

4.1.2.1 Macrograph of weld bead profile:

Figure 4.1 shows the macrograph of the cross-section of the weld bead that appeared during pulsed current GTAW where all three regions (1. base metal, 2. HAZ and 3. weld zone) were identified and marked for clarity. The macrograph was captured using the low-magnification stereo microscope for analyzing the weld bead profile. The solidification after welding was driven by epitaxial growth, i.e., solidification started following previously melted grains. Because of epitaxial growth during solidification, a very clear fusion boundary is difficult to observe [29]. The fusion boundary in Figure 4.1 was highlighted using interpolation and macro-etching of specimen. The grain growth and microstructural variation in HAZ from base, a clear distinguishable boundary was observed at the HAZ-base interface.

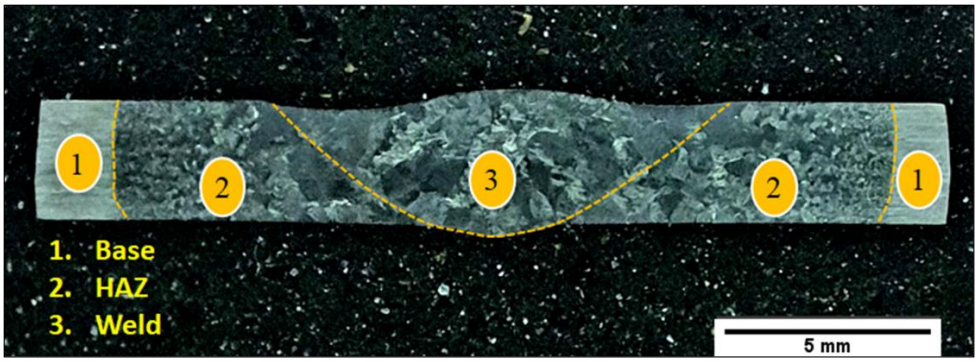

Figure 4.1 Weld bead profile appeared on Ti-6Al-4V alloy using pulsed-GTAW

4.1.2.2 Microstructure of base metal

The microstructure of as-received specimens was captured from prepared metallographic specimens. Figure 4.2 shows the microstructure of the as-received base Ti-6Al-4V alloy. The base Ti-6Al-4V had a very fine bi-modal microstructure, with grains that were an average of 4.2 μm in size. It was a typical dual-phase (α+β) alloy, with the bright α-phase growing evenly as equiaxed and elongated grains in the β-phase matrix. The dark β-phase in the base microstructure was clearly visible, which was either present at the grain boundary of the α-phase or inside the large α-grains.

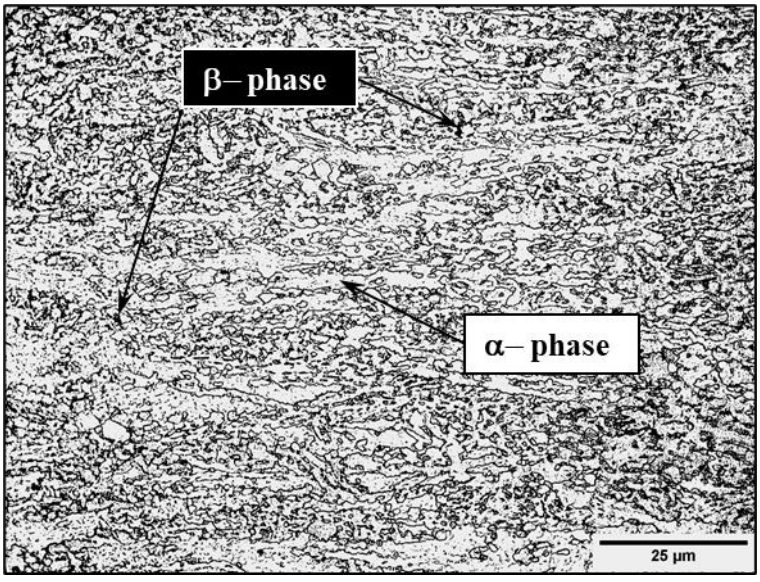

Figure 4.2 Microstructure of as received Ti-6Al-4V alloy

4.1.2.3 Microstructure of weld and HAZ

Figure 4.3 (a, b) shows the microstructure of the HAZ and weld region of Ti-6Al-4V alloy appeared using conventional-GTAW and Figure 4.3 (c, d) shows the microstructure of the HAZ and weld region of Ti-6Al-4V alloy appeared using pulsed-GTAW. The grain coarsening was observed in the HAZ and weld regions in both conventional and pulsed-GTAW. The HAZ near the base region is known as far-HAZ, and the region near the fusion zone is known as near-HAZ. In both the cases, conventional and pulsed-GTAW, grain coarsening in the HAZ was increasing from the near-HAZ to the far-HAZ. The prior-β grain boundaries were observed in the entire region of HAZ, which signifies that the temperature in HAZ was reached above the β-trans temperature.

In both cases, similar to HAZ, grain coarsening was observed in the weld region, and large prior-β grains appeared. Grain coarsening occurred primarily due to the high heat input and low thermal conductivity (7 W/m-k) of Ti-6Al-4V [5]. However, the presence of the secondary phase (β-phase) limits grain coarsening in both regions in comparison to α-titanium alloys [29]. The HAZ appeared using pulsed GTAW had finer prior-β grains (with an average grain size of 37 μm) in comparison to prior-β grains (with an average grain size of 60 μm) of HAZ appeared using conventional GTAW. Similar to HAZ grain refinement was also observed in the weld region produced using pulsed-GTAW in comparison to conventional-GTAW, and finer prior-β grains (with an average grain size of 105 μm) were obtained with pulsed-GTAW in comparison to prior-β grains (with an average grain size of 165 μm) obtained with to conventional-GTAW.

Grain refinement appeared using pulsed-GTAW was due to the switching of welding current from peak current to background current, where melting takes place during peak current and solidification takes place during background current. This intermittent melting and solidification led to grain refinement using pulsed GTAW. When the dark hatch like structure appeared inside the prior-β grains of HAZ and the weld was visualized at high magnification, they appeared as the fine acicular-α laths. Because of the fast rate of cooling during welding, the acicular-α appeared as a fine needle-like morphology inside the prior-β grains. The current pulsing during GTAW did not contribute much to the refinement of the acicular-α inside the prior β grains. Normally, very little or no martensite appears during GTAW of titanium alloys due to the relatively slower cooling rate compared to laser beam welding (LBW) and electron beam welding (EBW), where a large amount of hard martensite appears in different regions [6, 29].

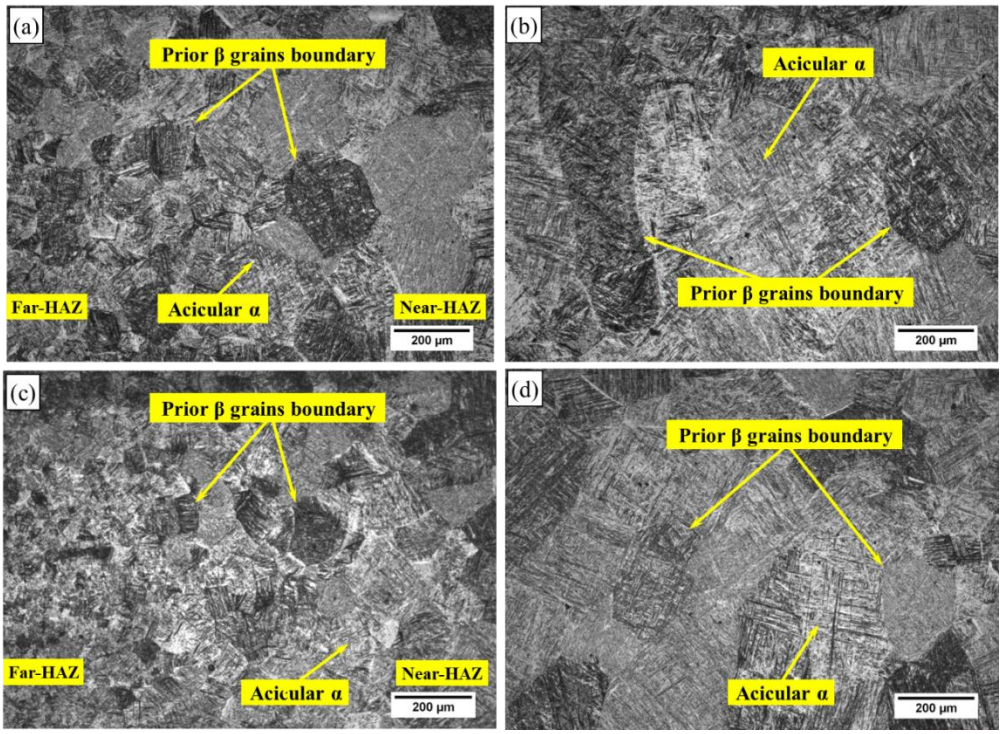

Figure 4.3 Microstructure of different regions of Ti-6Al-4V weldment: (a) HAZ of weldment prepared using conventional-GTAW; (b) weld region of weldment prepared using conventional-GTAW; (c) HAZ of weldment prepared using pulsed-GTAW; (d) weld region of weldment prepared using pulsed-GTAW

4.1.2.4 High magnification microstructure of weld and HAZ

The maximum temperature reached in the HAZ and weld zones exceeds the β-transus temperature and the typical cooling rate that prevails during the pulsed-GTAW process, the Widmanstätten morphology appears inside the prior-β grains in the heat-affected zone (HAZ) and weld zone [23]. Figure 4.4 (a) shows the microstructure of HAZ at low magnification, where prior-β grains can be seen and a few grain boundaries are highlighted. The size of prior-β grains in the HAZ near the fusion boundary is 65 µm ±10, which is decreasing from 65 µm near the fusion boundary to 15 µm near the base-HAZ boundary (refer to Figure 4.3 (a)). This can be understood in the sense that the part of the HAZ near the fusion zone was exposed to higher temperatures in comparison to the region of the HAZ away from the fusion boundary, which led to grain coarsening. Figure 4.3 (c) depicts the microstructure of the weld zone, where a few grain boundaries of prior-β grains are highlighted. The prior-β grains of HAZ and weld zone are filled with very fine lath morphology α-phase. High magnification images of HAZ and weld zone in Figures 4.4 (b) and 4.4 (d) show that the α-phase inside the prior-β grains has grown as a mixture of fine acicular and Widmanstätten basket weave type morphology. Finer lath morphology was observed in the weld zone (with an average lath size of 0.41 µm in width and 13 µm long) in comparison to HAZ (with an average lath size of 0.74 µm in width and 9 µm long). Weld zones have a high rate of cooling due to the high temperature gradient, which leads to finer morphology in this region [108, 121]. Similar morphology was observed in the weldment prepared using conventional GTAW, except finer morphology was observed with pulsed-GTAW weld. Finer morphology in the weld regions helps in obtaining better morphology dependent mechanical properties in the weld zone.

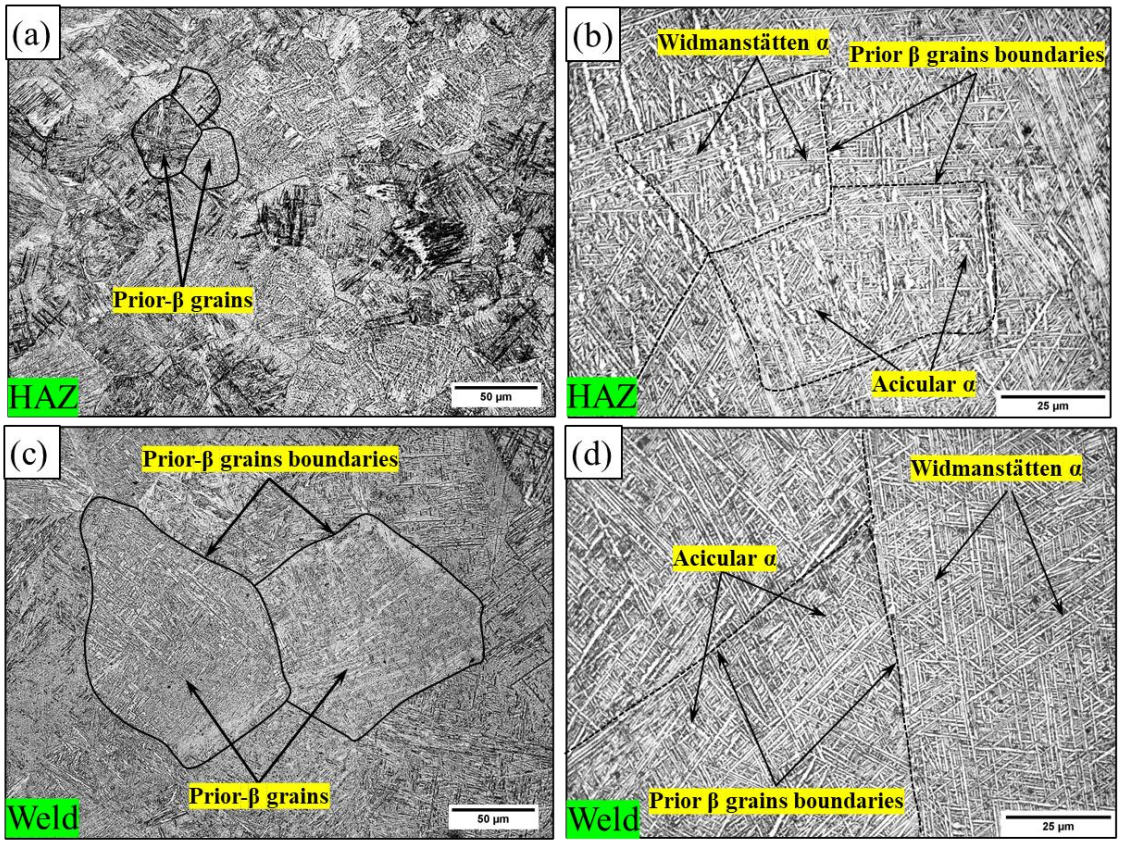

Figure 4.4 Microstructure of different regions of Ti-6Al-4V weldment: at low magnification (a) HAZ; (c) weld zone; and at high magnification (b) HAZ; (d) weld zone

4.1.3 Microhardness variation across the weld of Ti-6Al-4V alloy

The microhardness measurement of weldment was carried out as per the scheme discussed in Section 3.8.4 in Chapter 3. The average of three values of hardness at a location was taken and plotted against the location of the indentation. Figure 4.5 shows the micro-hardness measurement across the weldment, where nearly symmetrical hardness was observed from the center of the weld to either side of the weld. The hardness variation followed an increase in hardness from the base metal to the maximum in the weld region, but a little dip was observed in the far HAZ. The decrease in hardness around the far-HAZ was attributed to grain coarsening in this region. Despite having a coarser grain structure in the weld region and near HAZ, an increase in hardness in the fusion zone was observed due to the appearance of fine acicular and Widmanstätten basket weave-type morphology of α-phase inside the

prior-β grains. The weld-HAZ interface has a relatively faster cooling rate than the HAZ-Base interface [121]. The faster cooling rate at the weld-HAZ interface promoted the formation of fine acicular-α and higher hardness in the near-HAZ region. The formation of finer prior-β grains and α-phase morphology with pulsed GTAW than conventional GTAW helped in obtaining high hardness in welds and near-HAZ regions. The maximum average hardness (372 $HV_{0.2}$) was observed in the fusion zone of pulsed-GTAW, and around 5% less average hardness (364 $HV_{0.2}$) was observed in the fusion zone of conventional-GTAW. The high hardness in the weld region provides high strength to the weld region, but far-HAZ is a matter of concern due to the reduction in hardness in that region.

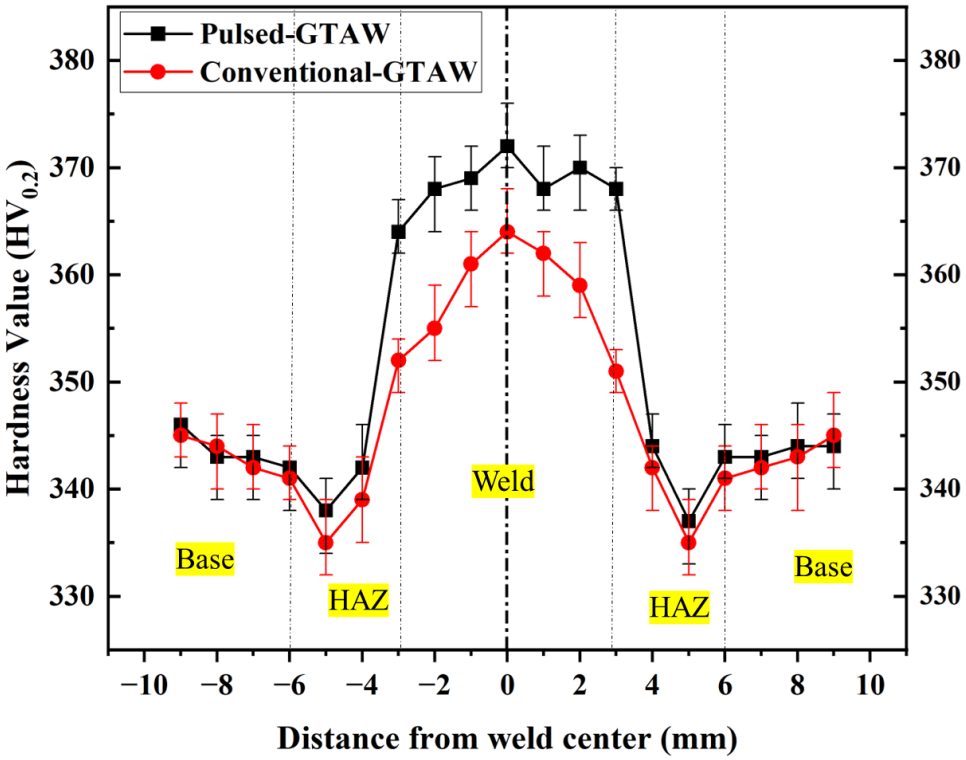

Figure 4.5 Hardness variation along the cross-section of weld in continuous and pulse GTAW

4.2 Effect of electrode tip angle on weld characteristics

In addition to the key welding parameters (welding current, welding speed, and arc voltage), the electrode tip angle also plays an important role in the weld bead

geometry during GTAW. An increase in electrode tip angle led to an increase in the energy density found at the anode and a decrease in the convective contribution of heat flux at the anode due to a reduction in gas velocity. The highest heat flux was observed in the range of 30° to 60° electrode tip angle during GTAW. The weld pool becomes unstable at extremely low electrode tip angles due to an increase in arc pressure and a decrease in arc length [10]. This study aims to understand the effect of the electrode tip angle on the weld bead geometry, depth of penetration, distortion, and hardness of pulsed gas tungsten arc welded 2 mm CP-Ti sheets. Defect-free titanium welds were prepared by using p-GTAW with the help of an indigenously developed shielding setup. The weld beads obtained using 30°, 45°, 60°, 75°, and 90° electrode tip angles were analyzed under a stereomicroscope. Measurements of different geometrical elements were performed using the 'Image-J' software. Optical microscopy, distortion measurement, and microhardness measurement were also performed to further assess the weld integrity of CP-Ti welds.

In this experimental work, bead-on-plate welding (BOP) has been performed on the 2 mm thick as-received CP-Ti sheets. The elemental weight percentage composition of the CP-Ti sheet is listed in Table 3.1. Coupons of 100×50 mm^2 dimensions were cut from CP-Ti sheet, and around 90 mm long weld beads were made at 250 mm/min welding speed. The different tip angles (such as 30°, 45°, 60°, 75°, and 90°) prepared on 2% thoriated 2.4 mm diameter tungsten electrodes, and utilized during the experiments are shown in Figure 3.6. P-GTAW was utilized for performing BOP welding on CP-Ti sheets. The pulse parameters were selected depending upon the trial experiments discussed in the Section 3.4. On the selected pulse parameters, welds were having maximum penetration and permissible undercut at reduced heat

input. The detailed list of welding parameters used during the experiments is listed in Table 4.1.

Table 4.1 Welding parameters

Parameters	**Value**
Shielding gas	Ar (99.99 % Pure)
Peak current (Ip)	148 A
Peak current (I_p)/Background current (I_b)	5/2
Background current time (T_b)/ Peak current time (T_p)	3/2
Pulsed frequency (f)	5 Hz
Welding speed (v)	250 mm/min
Voltage (V)	10-11 V
Pre-flow time (Shielding gas)	10 s
Post-flow time (Shielding gas)	15 s
Electrode diameter (Thoriated 2%)	2.4 mm
Electrode tip angle	30°, 45°, 60°, 75°, and 90°
Gas flow rate	18 l/min

The current level for BOP welding was selected in such a way that full penetration should not occur at the electrode tip angle, which helped in observing the effect of the electrode tip angle on various geometrical elements. The distortions that appeared in the welded specimen were measured using a Mitutoyo 2046S 10 mm mechanical dial gauge. Later, the weld beads were cut cross-sectionally, and metallography studies and hardness measurements were performed on mirror-polished samples as per the scheme discussed in Sections 3.8.2 and 3.8.4. The captured weld bead profile and weld geometrical elements were measured using 'Image-J' software. Phase analysis of the as-received material and welded specimen was observed using a Rigaku Miniflex 600 X-ray diffractometer at a 10°–90° scan angle.

4.2.1 Effect of different electrode tip angle on weld bead appearance

Figure 4.6 (a-e) shows the top and root of the bead on a plate weld produced using 30°, 45°, 60°, 75°, and 90° electrode tip angles, respectively. The shielding set-up used during BOP welding worked well, and the weld beads obtained had a silvery colour on either side. The straw and dark blue colours that appeared away from the weld bead do not affect the weld quality, as these colours appeared after the weld reached to the room temperature and came into contact with the atmosphere [22, 122]. The samples were analyzed using X-ray radiography, and the samples successfully met the X-ray radiographic standards. The electrode tip angle played a major role in the geometrical elements of the weld due to the arc constriction caused by increasing the electrode tip angle [78]. An increase in the electrode tip angle shrinks the arc diameter and increases the number of electrons density. Due to the shrinkage in the arc diameter, the increase in the anode current density and heat flux is referred to as arc constriction in GTAW [14, 78]. The effect of arc constriction could be observed from the top region of the weld. The width of the weld bead decreases as the electrode tip angle increases. The weld bead width corresponding to the different electrode tip angle has been listed in Table 4.2. The measurement of other geometrical elements of the weld and its relationship with the electrode tip angle have been discussed later.

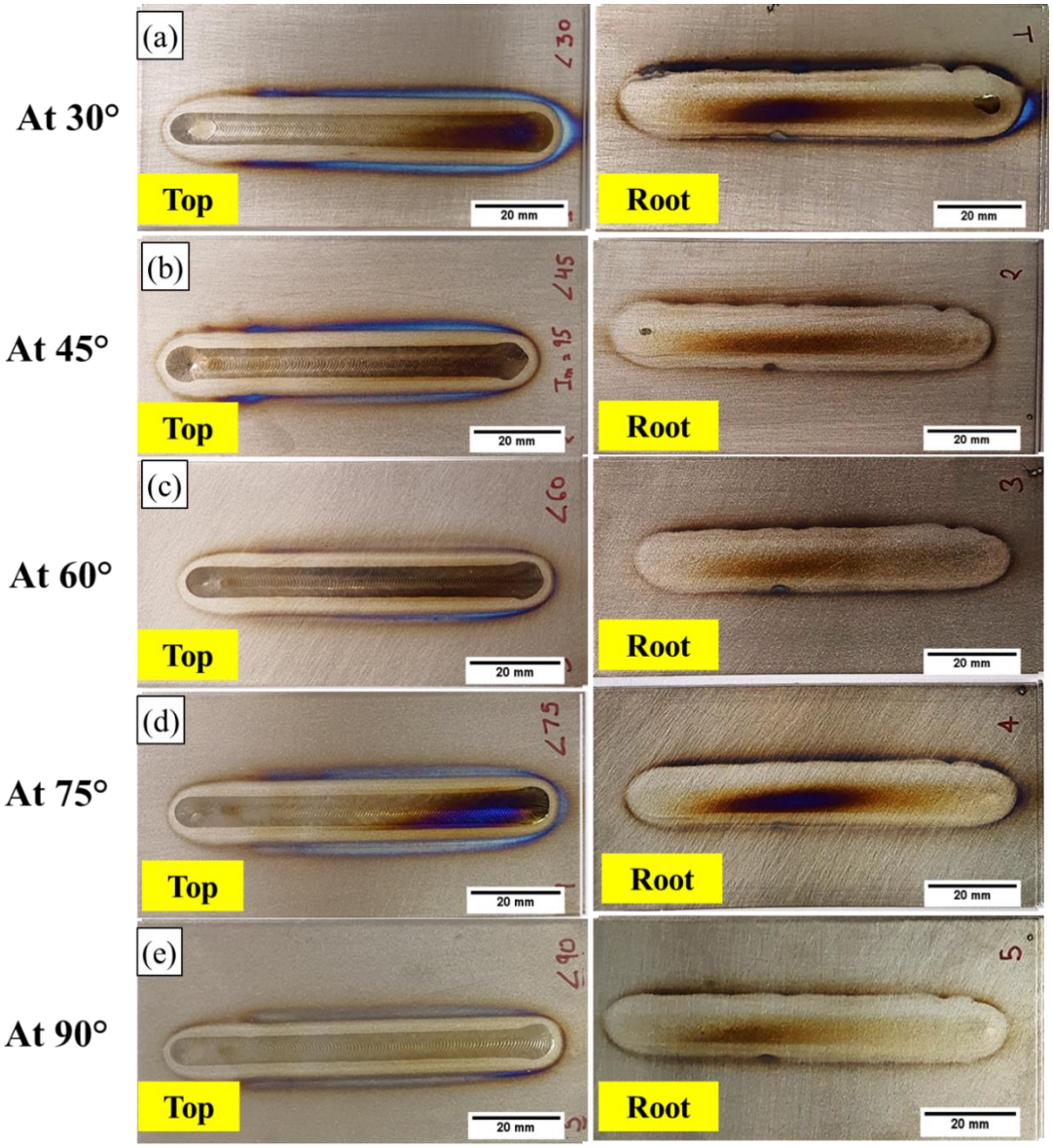

Figure 4.6 Top and root of the BOP welding on CP-Ti using (a) 30°; (b) 45°; (c) 60°; (d) 75°, and (e) 90° electrode tip angles

Table 4.2 Measurement of weld bead width with respect to different electrode tip angles

Electrode tip angle (degrees)	Weld bead width
30°	6.84
45°	6.72
60°	6.33
75°	6.20
90°	5.32

4.2.2 Microstructure of different regions weldment at 60° tip angle

Figure 4.7 shows the microstructure of the base, HAZ, and fusion zone of the weld prepared using a 60° electrode tip angle. Figure 6 (a) depicts the microstructure of the CP-Ti base, a single phase α-titanium alloy with an equiaxed morphology. Figure

4.7 (b) depicts the microstructure of base-HAZ boundary (near-HAZ), which was identified by looking at the microstructural changes that appeared due to the weld thermal cycle. Figure 4.7 (c) shows the microstructure of far-HAZ, where large prior-β grains were observed. The prior-β grains in HAZ show that the temperature of HAZ has reached above β-transus temperature. The coarsening of prior-β grains took place due to the low thermal conductivity and the absence of a secondary phase in the CP-Ti. The grain coarsening continued from the near-HAZ to the weld region [24]. Figure 4.7(d) shows the microstructure of the weld region, where large (up to 1.5 mm) prior-β grains were observed. Unlike the Widmanstätten morphology that appeared inside the prior-β grains in α-β titanium, here only acicular α could be observed inside the prior-β grains. The weld region had the maximum fraction of acicular α, and the amount is decreasing from weld to near-HAZ due to a decrease in temperature gradient and cooling rate.

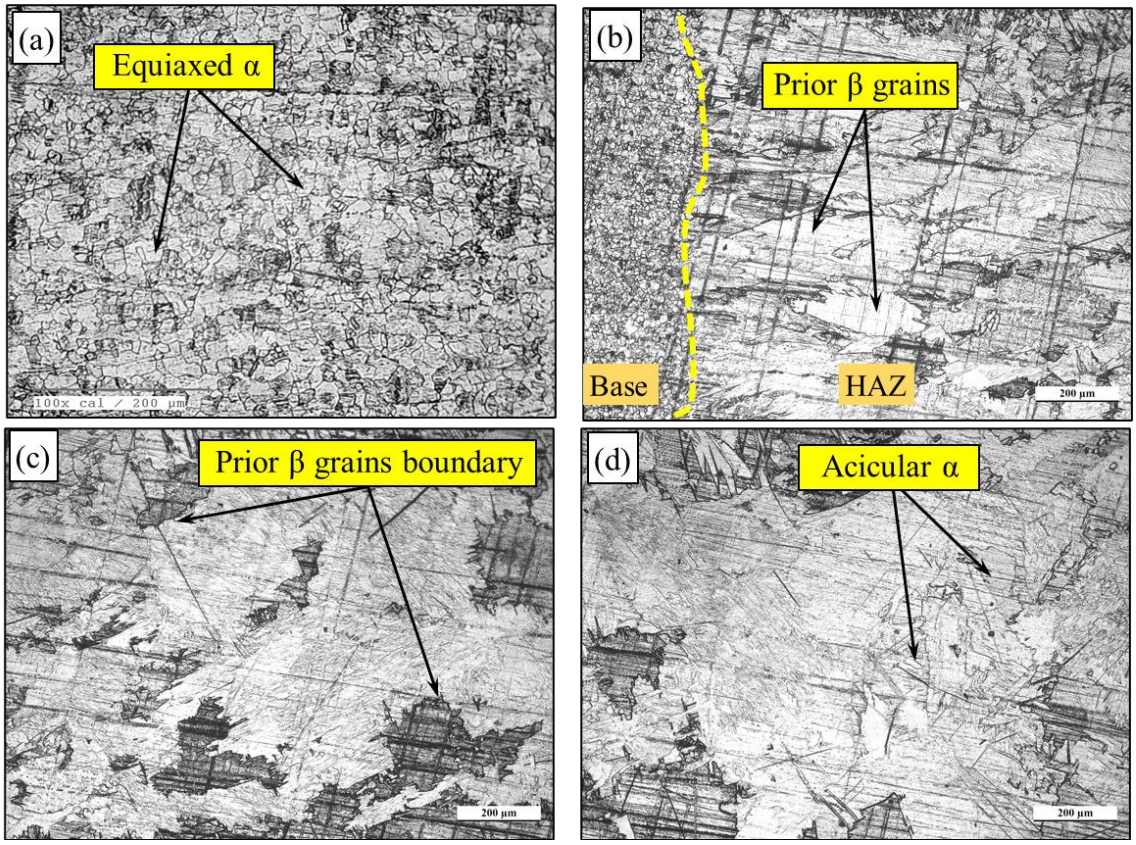

Figure 4.7 Microstructure of the different regions of weld: (a) base CP-Ti; (b) near-HAZ; (c) far-HAZ; (d) weld region

4.2.3 Effect of electrode tip angle on various weld geometric elements

Figure 4.8 (a-e) shows the macrographs of the weld bead cross-sections of the weldments produced using 30°, 45°, 60°, 75°, and 90° electrode tip angles, respectively. The macrographs were captured using a stereomicroscope. The HAZ-base boundary was easily distinguishable, and it could be observed in any metallographic sample of CP-Ti, but to reveal the HAZ-fusion boundary, samples were macro-etched using concentrated etchant (details mentioned in Section 3.8.2) for increased time. The fusion boundary is highlighted in the figures for better clarity, and the measurement of bead width and depth of penetration was performed using 'Image J' software. For better clarity, the measurements of the weld geometrical elements are also labelled on the weld bead cross-section.

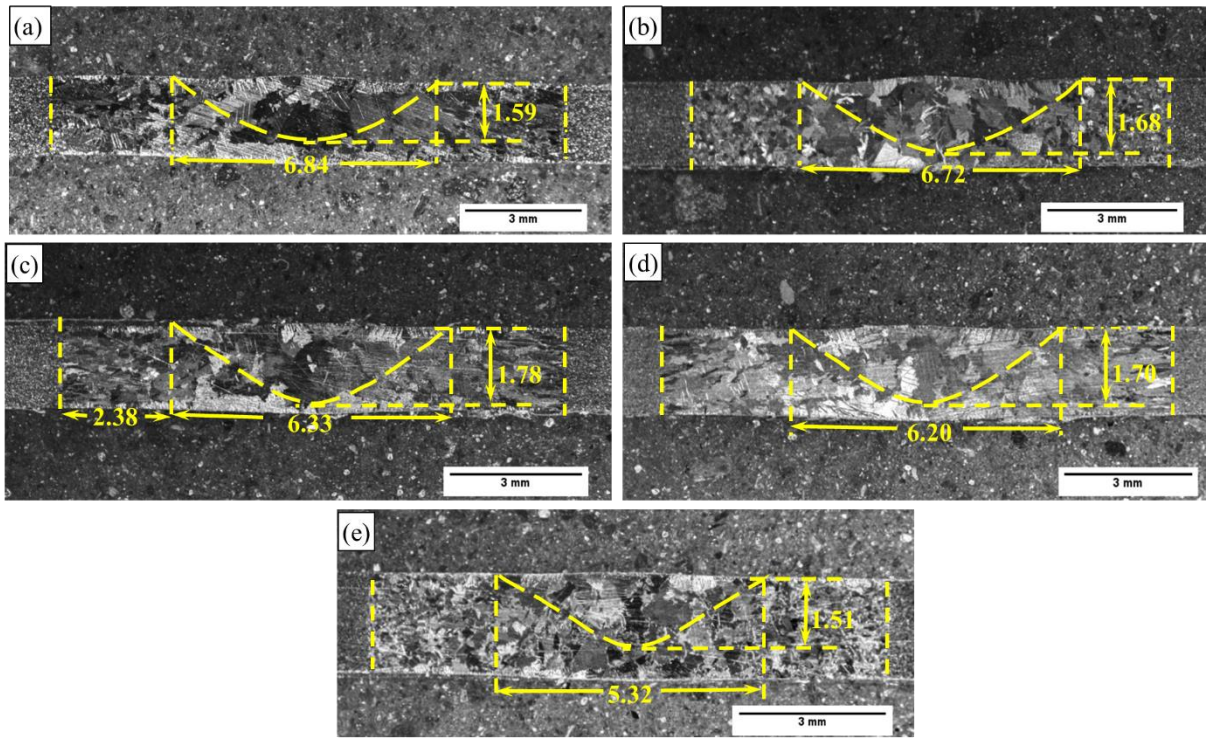

Figure 4.8 Weld bead profiles at different electrode tip angles: (a) at 30°; (b) at 45°, (c) at 60°, (d) at 75°, (e) at 90°

Figure 4.9(a and b) shows the effect of electrode tip angle on bead width and penetration, respectively. In Figure 4.9(a), on increasing the electrode tip angle from 30° to 90°, the bead width decreased from 6.84 mm to 5.32 mm with the increase in the electrode tip angle due to arc constriction. In Figure 4.9(b), an increase in weld penetration was observed from 1.59 mm to 1.75 mm, with an increase in electrode tip angle from 30° to 60. However, upon further increasing the electrode tip angle from 60° to 90°, the weld penetration began to decrease from its maximum level. This was because of the increase in resultant heat flux on increasing the electrode tip angle from 30° to 60° due to arc constriction. But with a further increase in electrode tip angle from 60° to 90°, the gas velocity increased, which increased the convective contribution of heat flux, and the resultant heat flux decreased. Because of the decrease in resultant heat flux, a decrease in depth of penetration was observed from 60° to 90° electrode tip angle [123]. The maximum depth of penetration was observed with 60° electrode top angle. The electrode tip angle of 60° for maximum

penetration fell within the range that other researchers have also observed for other materials [78, 123].

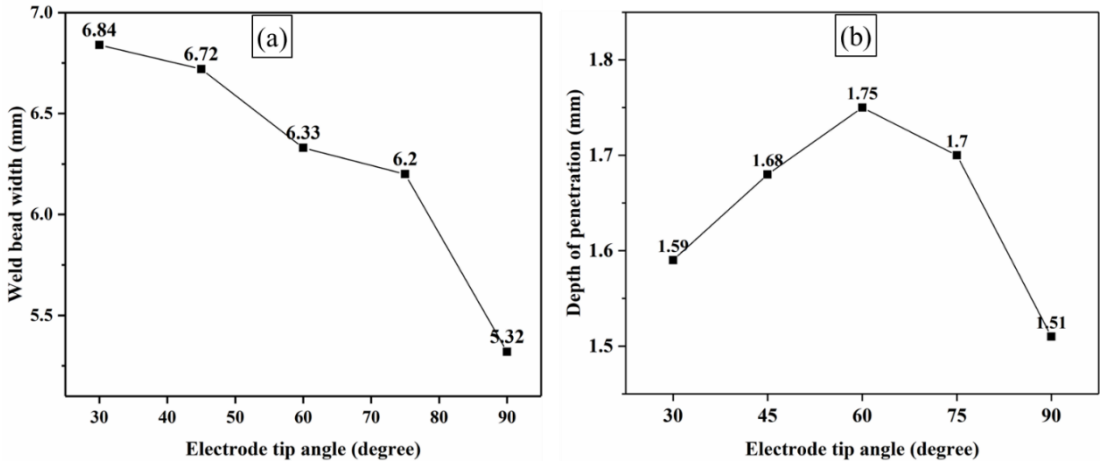

Figure 4.9 Effect of electrode tip angles on: (a) bead width; (b) depth of penetration

4.2.4 Effect of electrode tip angle on weld distortion

BOP welding at different tip angle was performed without clamping the plates, i.e., plates were allowed to distort due to the weld thermal cycle, and the effect of electrode tip angle on distortion was observed. Depending on the type of shrinkage, the distortion in the weldment can be divided into longitudinal and transverse distortions. The distortions that appeared in weldments were measured using a mechanical dial gauge, as shown in Figure 4.10 (a). Distortion measurements were recorded at an interval of 5 mm in the longitudinal and transverse directions. The welded plate was firmly clamped, and the dial gauge was rested on the surface plate for distortion measurement. The clamping location was different for transverse and longitudinal distortions, for transverse distortion, the location of clamping was away from the weld and near the center line of the weld, and for longitudinal distortion, it was away from the weld center line and middle of the weld. The location of the clamping at different tip angles was within the range of the width of the weld. Figure

4.10 (b, c) shows the effect of electrode tip angle on transverse and longitudinal distortion in the weldment. The distortions were increasing from the center to the edges in both cases. Figure 4.10 (d) and (e) show the maximum average transverse and longitudinal distortion and angular distortion, respectively, that occurred with different electrode tip angles. The maximum transverse distortion (0.21 mm) was observed for the 30° tip angle, and the maximum longitudinal distortion (0.12 mm) was observed for the 30° and 45° electrode tip angles. An increase in tip angles generally leads to a reduction in distortion. The sheet welded using a 90° electrode tip angle had the minimum distortion. However, welds prepared using a 60° electrode tip angle had permissible distortion and a maximum depth of penetration (refer to Figure 4.9 (b)). For the testing range of the electrode tip angle, the average transverse distortion was greater than the average longitudinal distortion, i.e., the transverse shrinkage predominated over the longitudinal shrinkage. Transverse distortion is greater than longitudinal distortion in welding due to localized thermal expansion and contraction across the weld's width, causing more shrinkage forces. The transverse direction has less restraint and stiffness than the longitudinal direction, leading to greater bending and deformation during cooling. By increasing the electrode tip angle, the width of the weld bead decreased, thereby reducing shrinkage in the weldment. The reduction in weld shrinkage led to a decrease in distortion in the weld [61, 124]. However, in the current experimentation, the welds have been prepared for approximately same weld penetration. Therefore, weld bead having larger bead width will have larger pool volume and consequently show larger distortion. The weld prepared using a 60° electrode tip angle has a good combination of relatively low and permissible distortion and maximum depth of penetration. Since, maximum penetration was obtained at 60° electrode tip angle and the

penetration was decreasing with increasing or decreasing electrode tip angle, the heat input required for welding would be minimal if the electrode tip angle is 60°. Therefore, a 60° electrode tip angle could be utilized for obtaining a sound weld at minimum heat input.

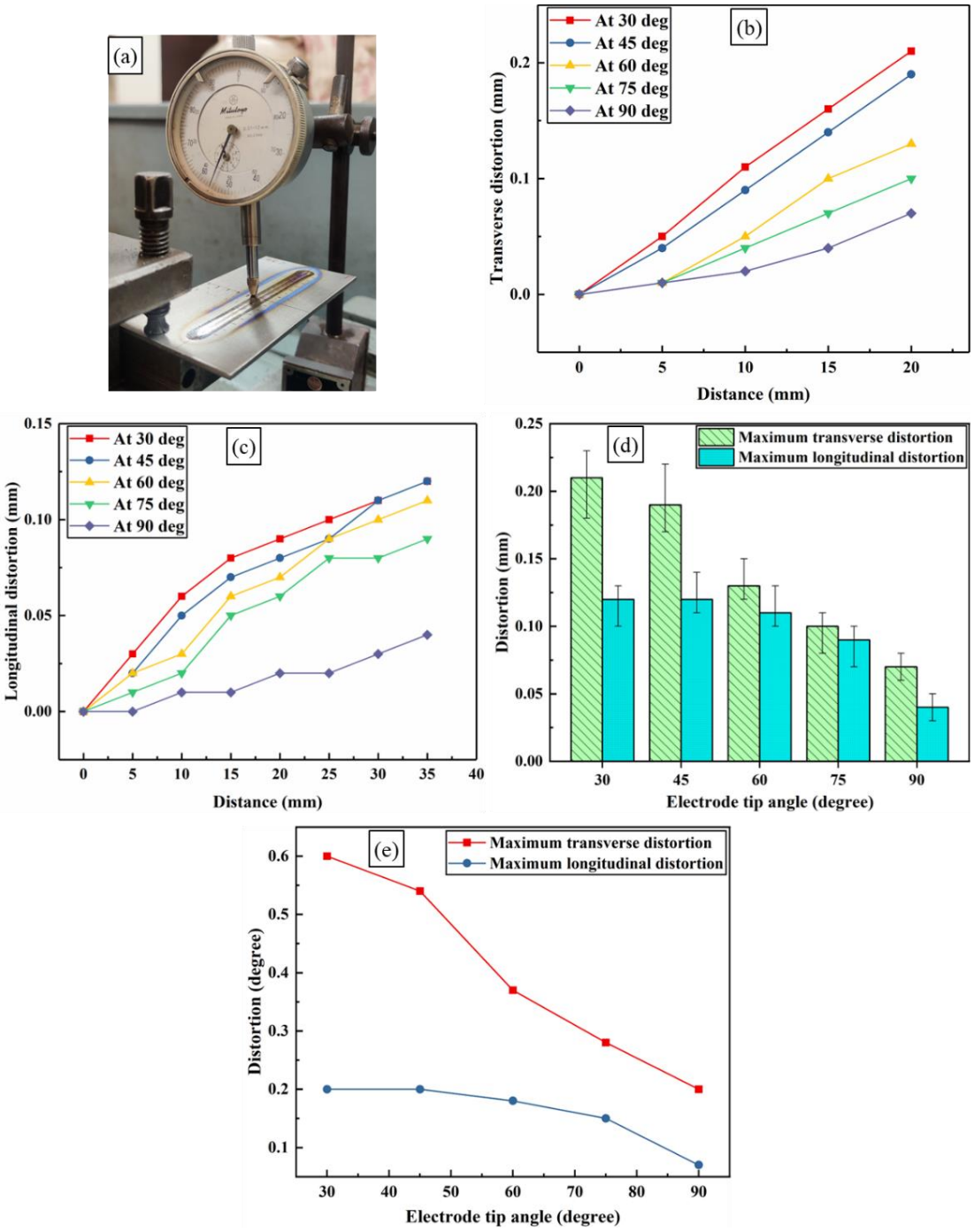

Figure 4.10 (a) Mechanical dial gauge with welded plate; (b) transverse distortion variation; (c) longitudinal distortion variation; (d) and (e) comparison between maximum average transverse and longitudinal distortion and angular distortion respectively with different electrode tip angles

4.2.5 Effect of electrode tip angle on microhardness variation

Microhardness measurements were conducted across the cross-section of the weldments prepared using various electrode tip angles. A similar trend of hardness was observed for the welds prepared using electrode tip angles of 30°, 45°, 60°, 75°, and 90°, with only slight variations. The different electrode tip angles cause different weld thermal cycles, cooling rates, and the consequent microstructural transformations and microhardness values in weld regions. Figure 4.11 (a) shows the plot of the average microhardness variation across the weldment prepared using a 60° electrode tip angle with respect to the location of the indentation. Figure 4.11 (b) shows the microhardness of the HAZ and weld region of weldment prepared using electrode tip angles of 30°, 45°, 60°, 75°, and 90°. The average hardness of the base CP-Ti was 141 $HV_{0.2}$, with very small variation. However, with increasing electrode tip angle, a slight increase in average microhardness was observed in the HAZ and weld regions. The increase in hardness is attributed to the arc constriction on increasing the electrode tip angle, leading to a narrower weld pool, which caused an increase in cooling rate and increased the chances of acicular morphology with a 90° electrode tip angle [5]. The maximum average hardness (151 $HV_{0.2}$) was obtained in the weld region of 90° tip angle weldment, while the minimum average hardness (134 $HV_{0.2}$) was observed in the HAZ of 30° electrode tip angle weldment. Despite the presence of coarse prior-β grains in the weld region, the high hardness observed in this region is attributed to the presence of fine acicular morphology of α-phase [124]. The fraction of fine acicular α decreased gradually from the weld region to the HAZ, resulting in the dominance of large prior-β grains in far-HAZ resulting in reduction of hardness in far-HAZ.

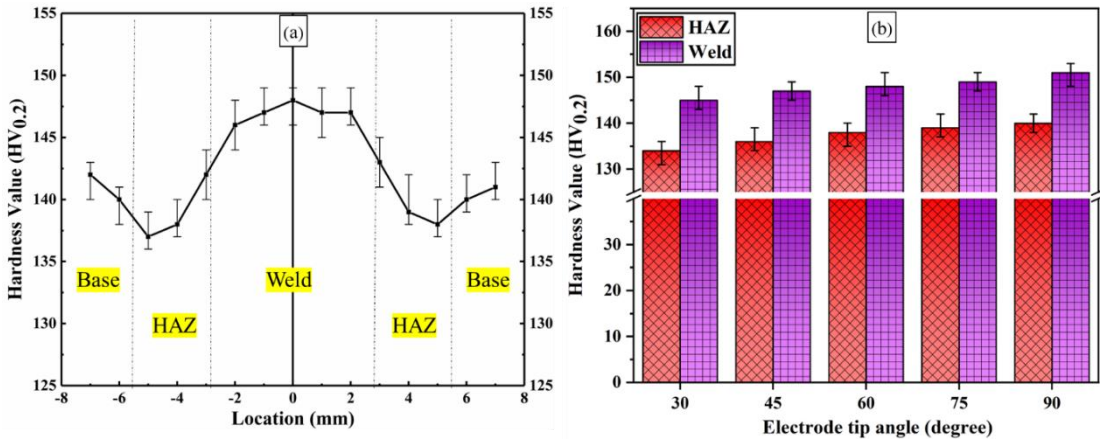

Figure 4.11 (a) Microhardness variation across the weld at 60° electrode tip angle; (b) microhardness of the HAZ and weld region at 30°, 45°, 60°, 75°, and 90°

4.2.6 X-ray diffraction analysis of as-received CP-Ti and welded specimen

X-ray diffraction analysis of the as-received CP-Ti and the weld specimens has been carried out to analyse the effectiveness of the shielding setup and compare the weld with the base metal. Figure 4.12 shows the XRD profiles obtained for the as-received CP-Ti and its weld. The major peaks of the XRD pattern for CP-Ti confirmed the presence of CP-Ti only, and a similar pattern was observed for the weld region with a diminished intensity of the peaks. The peak intensities depend on the morphology present in the material, and a reduction in peak intensities indicates the conversion of fine globular or equiaxed morphology α-phase to large plate-like and needle-like morphology [125]. The weld metal, heat-affected zone (HAZ), and base metal also experience distinct temperatures and cooling rates, causing differences in grain size and phase distribution. This conversion could also be seen in the microstructural change in the weld region from the as-received base CP-Ti, where the morphology of the weld region has been converted into large plate-like alpha and fine acicular alpha from the equiaxed morphology of base CP-Ti (section 4.2.3). There was no peak observed corresponding to any oxide of titanium in the welded sample, which

confirmed that the shielding set-up successfully protected the weldment from atmospheric contamination.

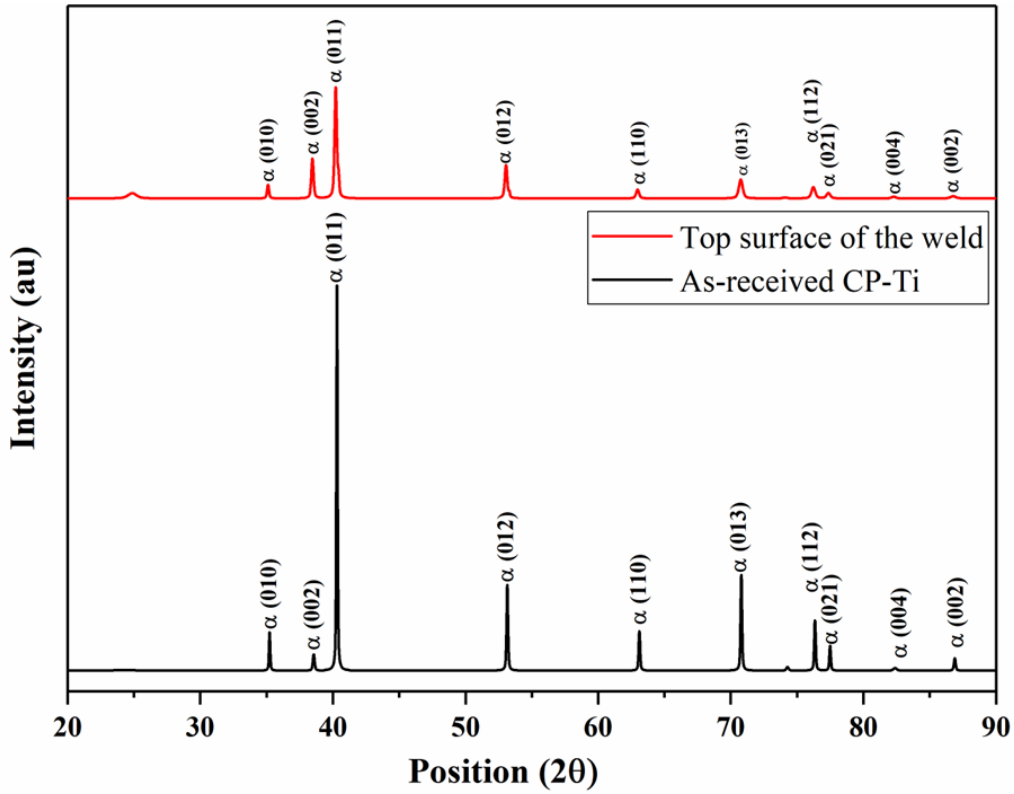

Figure 4.12 XRD pattern obtained for as-received CP-Ti and the top surface of the weld

4.3 Effect of different current pulsing parameters on weld bead profile

GTAW is a versatile welding method, and almost all the metals and their alloys could be welded [14]. However, several limitations, like low penetration, wide weld bead, and grain coarsening in HAZ and weld regions during conventional GTAW, could be avoided by selecting the correct pulsed parameters during welding. The p-GTAW offers many advantages, like large weld bead penetration at low heat input, grain refinement in the weld and HAZ regions, reduction in weld bead width, and reduction in weld distortion [126]. Additionally, the p-GTAW has superior control over the heat input, making it easier to employ this technique for precise work [73]. In this section, the effect of individual current pulsing parameters other than pulse

frequency on the weld bead profile during GTAW was studied. The effects of changes in background current percentage and changes in background current time were studied and compared with conventional GTAW. The current level for the experiments was selected in such a way that the effect of pulse parameters on weld penetration and weld bead width could be visually observed. The weld beads were cut cross-sectionally, and the weld profile at different pulse parameters was analysed through the measurements using “ImageJ”. The effects of changes in background current time on weld penetration and reduction in weld bead width dominated over the changes in background current with the same percentage.

Table 4.3 List of pulsed parameters used for different experiment

Exp.	I_m	I_P	I_b (% I_p)	t_p	t_b	f	V
1	100	--	--	--	--	--	11
2	100	147	50	50	50	5	11.5
3	100	157	50	40	60	5	11.5
4	100	169	50	30	70	5	11.5
5	100	157	40	50	50	5	11.5
6	100	172	40	40	60	5	11.4
7	100	189	40	30	70	5	11.2
8	100	170	30	50	50	5	11.2

The BOP welding was carried out on 2 mm thick CP-Ti sheets with the help of an indigenously developed shielding set-up and using conventional and pulsed GTAW. The weld beads were prepared at a constant mean current (100 A), frequency (5 Hz) and welding speed (250 mm/min) with varying percentages of background current (Ib) and background current time (tb). Two-step background current and three-step background current time were varied in steps of 10 percent change. The complete list of pulsed parameters used for different experiments has been mentioned in Table 4.2, where the background current time percentage was varied from 50 to 70 percent and

the background current was changed from 50 to 40 percent. The peak current for each pulse parameter set was adjusted according to the weighted average formula discussed in Section 1.3, keeping the mean current constant and listed in Table 4.2. Other than the above-discussed welding parameters, they were selected as discussed in Tables 3.6 and 3.7 in Section 3.7.2. Metallographic specimens were prepared as per the ASTM E407 standard and etched as per the procedure discussed in Section 3.8.2 for stereomicroscopy. To obtain the pulse parameters for sound weld profile, i.e., with maximum penetration with permissible limit of hump and undercuts at minimum heat input. The systematic experiments at different pulse parameters have been performed to observe the effect of different pulse parameters on different geometrical elements and select pulse parameters for final experimentation, where humps and undercuts must be within permissible limit. The measurement of different weld bead profile parameters discussed in Figure 4.13 was done using 'ImageJ' software.

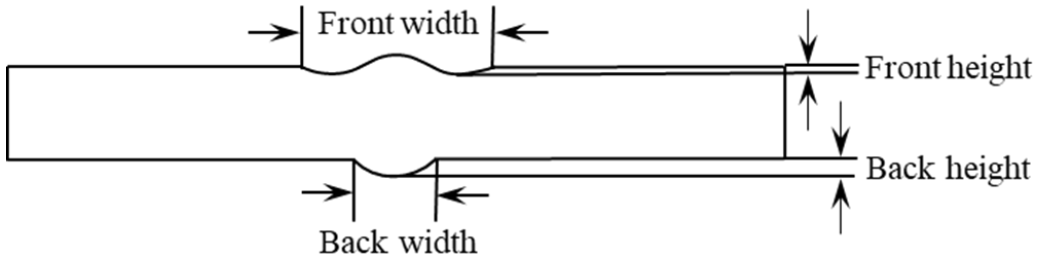

Figure 4.13 Weld bead profile parameters

4.3.1 Weld bead appearance at different pulse parameters

Figure 4.14 shows the weld bead appearance at different sets of pulse parameters. Each set of pulse parameters in Table 4.2 denotes an experiment. The first experiment was performed without pulsing the current at 100 A, keeping the other parameters fixed as discussed in Table 3.5. It can be observed from experiment one that through-thickness melting or full penetration was not achieved with this

parameter set. Experiment two was performed using pulsed current, keeping the background current (I_b) level at 50 percent of the peak current (I_p) and maintaining an equal percentage (50%-50%) for the time for peak current (t_p) and the time for background current (t_b). In this experiment, through-thickness melting was not achieved. However, when 't_b' was increased by 10%, the value of peak current increased due to the weighted average, leading to increased arc intensity and achieving through-thickness melting. In experiment 4, a further increase in 't_b' led to more melting, as observed from the broader back width. Further increase in 't_b' led to destabilize the arc, affecting continuous melting. In experiment 5, 'I_b' was decreased by 10%, and 'tp' and 'tb' were kept equal (50% - 50%). In this case, very little through-thickness melting was observed compared to experiment 3, where 'tb' was increased by 10%. This shows that the effect of increasing 'tb' dominates over the decrease in 'I_b' by the same percentage at constant mean current. Experiments 6 and 7 show the same trend as experiments 3 and 4, with increased 'tb' resulting in slightly more melting, as observed from the increased back width. When the background current percentage was further decreased from 40% of 'I_p' to 30% of 'I_p,' intermittent non-through melting and burning were observed depicted using experiment 8.

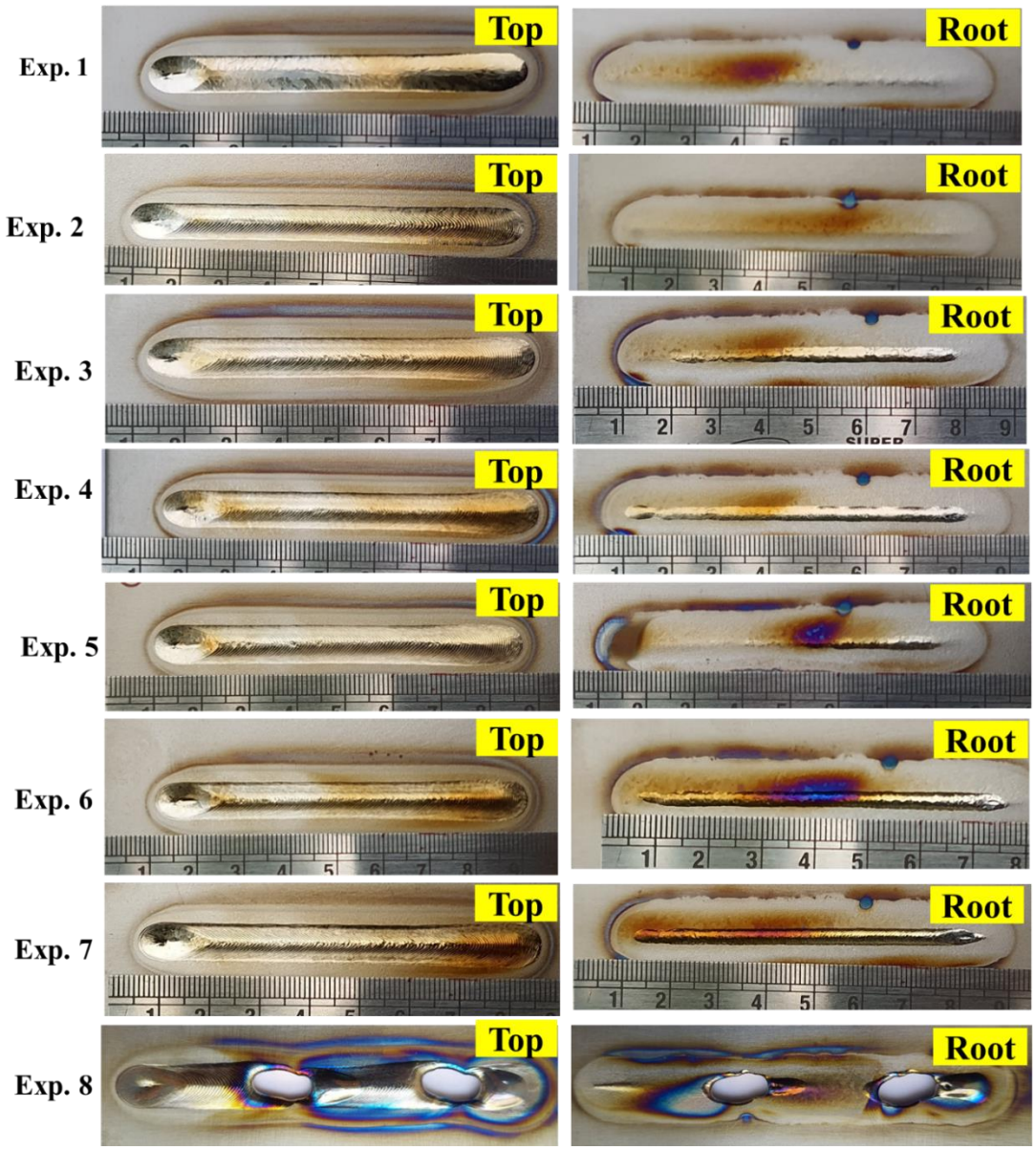

Figure 4.14 Weld bead appearance at different set of pulse parameters

4.3.2 Weld bead profile measurement

Figure 4.15 shows the weld bead profiles at different sets of pulsed parameters listed in Table 4.2. Weld bead profiles are highlighted for better clarity. As discussed in the previous section, through-thickness melting was not achieved in experiments 1 and 2, as evidenced by the weld profiles for these experiments. However, an improvement in depth of penetration from 1.76 mm to 1.8 mm was observed with pulsed current GTAW compared to conventional GTAW at the same heat input. Through-thickness

melting was observed in experiments 3 to 7, with the back width increasing with the increase in time for background current.

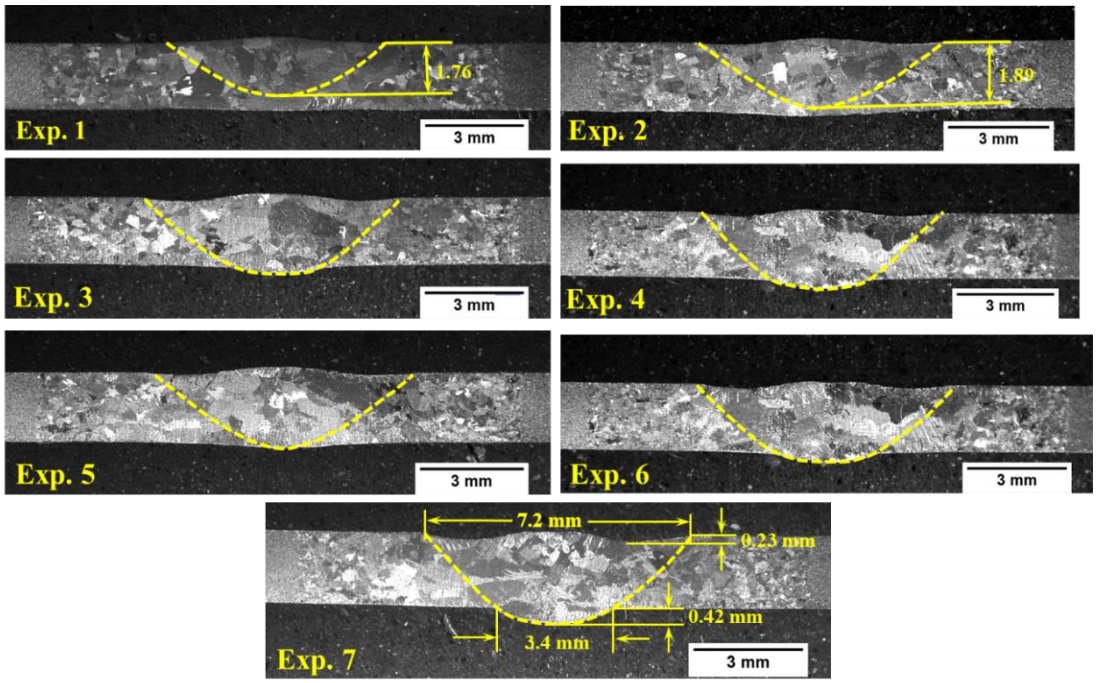

Figure 4.15 Weld bead profiles and their measurement for different set of pulse parameters

The measurement of different weld bead profile parameters (such as depth of penetration, front width, back width, front height, and back height) shown in Figure 4.13 was performed using 'ImageJ' software. All the measurements of the weld bead profile are listed in Table 4.3. The initial increase in front width occurred from 6.9 mm to 7.4 mm in the transition from experiment 1 to experiment 2, where the welding process shifted from conventional GTAW to pulsed GTAW due to a rise in high peak current. However, with the subsequent increase in 'tb' during experiments 2 to 4 and 5 to 7, the front width decreased, resulting in a narrower weld bead. A similar trend was observed for the back width, which increased from experiments 2 to 4 and 5 to 7, while an opposite trend was observed for the front height and back height. The set of pulse parameters in experiment 7 shows maximum penetration at

minimum heat input and is used for subsequent dissimilar titanium alloy (CP-Ti/Ti-6Al-4V) welding.

Table 4.4 Weld bead profile parameter measurement at different set of pulse parameters

Exp.	Depth of Penetration	Front width	Back width	Front height	Back height
1	1.76 ± 0.06	6.9 ± 0.02	--	0.22 ± 0.02	--
2	1.89 ± 0.05	7.4 ± 0.01	--	0.11 ± 0.01	--
3	Full penetration	7.3 ± 0.01	2.96 ± 0.01	0.14 ± 0.01	0.24 ± 0.02
4	Full penetration	7.2 ± 0.02	3.16 ± 0.02	0.15 ± 0.02	0.30 ± 0.03
5	Full penetration	7.4 ± 0.01	0.8 ± 0.01	0.11 ± 0.01	0.10 ± 0.02
6	Full penetration	7.1 ± 0.01	3.3 ± 0.02	0.17 ± 0.01	0.31 ± 0.03
7	Full penetration	7.2 ± 0.02	3.4 ± 0.02	0.23 ± 0.02	0.42 ± 0.02

4.4 Dissimilar welding of titanium alloys (CP-Ti/Ti-6Al-4V) using pulsed GTAW

In this section, the dissimilar welding of titanium alloys (CP-Ti (α-alloy-grade 2)/Ti-6Al-4V (α+β-alloy-grade 5)) was performed autogenously with the help of an indigenously designed and developed shielding setup, utilizing conventional and pulsed GTAW processes at varying frequencies. Dissimilar welding was performed on 2 mm thick CP-Ti and Ti-6Al-4V sheets in as-received condition using pulsed GTAW at varying pulse frequencies (from 3 Hz to 5 Hz in steps of 0.5 Hz) and compared with conventional GTAW. The chemical compositions (wt.%) of the materials are listed in Table 3.1. Coupons of 100 × 50 × 2 mm^3 dimensions were cleaned, and square flat edges at the butt-welding side were prepared as per the procedure discussed in Section 3.7.1. Pure argon (99.99%) gas was used as the shielding gas during the dissimilar welding of these alloys. The dissimilar welds were produced as per the procedure discussed in Section 3.7.3 (preparation of dissimilar weld) and using the welding parameters listed in Tables 3.7 and 3.8. The mean current for pulsed and conventional GTAW was kept the same to maintain

nearly the same heat input. Prepared welds were visually analyzed and underwent X-ray radiographic analysis. Samples for metallographic studies were prepared as discussed in Section 3.8.2. X-ray diffraction analysis was carried out for phase analysis in the weld region after dissimilar welding. Energy dispersive spectroscopy (EDS) analysis was conducted across the weld at different locations. Mechanical testing, such as microhardness measurement, tensile testing, impact testing, and impression creep analysis, was carried out on dissimilar welded titanium alloys. The impression creep analysis was performed in different regions (base, HAZ, and weld) of the weldment to study the high-temperature behaviour of each region. The details of sample preparation and testing schemes for mechanical tests are discussed in Sections 3.8.5 to 3.8.8. The fractured tensile and impact specimens were analyzed under a scanning electron microscope (SEM). All the equipment and techniques utilized for characterizing the dissimilar weld are detailed in Section 3.8.

4.4.1 Weld prepared using conventional and pulsed GTAW at different frequencies

The dissimilar welding of titanium alloys (CP-Ti/Ti-6Al-4V) was performed at different frequencies using pulsed-GTAW and conventional-GTAW. Figure 3.16 shows the weld bead appearance using conventional-GTAW and pulsed-GTAW at frequencies from 3 Hz to 5 Hz with intervals of 0.5 Hz. The heat input rate is independent of pulse frequency. However, changing the pulse frequency alters the time for peak current and background current, affecting both the weld geometry and mechanical properties. The frequency was varied to evaluate its impact on weld geometry and mechanical properties. It was adjusted in 0.5 Hz intervals, as the effect of pulse frequency was significant within a narrow range. These welds were prepared

with the help of an indigenously developed shielding setup and were free from atmospheric contamination, exhibiting a silvery bright colour on either end [22].

Based on the weld bead appearance, all the welds exhibited a silvery bright colour, indicating they were free from atmospheric contamination and acceptable. However, weld beads produced at different frequencies showed variations in ripple appearance. A smooth, flat bead was obtained with conventional GTAW, while ripples became finer and the weld bead narrower as the frequency increased from 3 Hz to 5 Hz. The increase in ripple intensity with pulse frequency contributed to microstructural refinement and influenced the mechanical properties of the dissimilar weld. *Balasubramanian et al. (2009)* found that increasing pulse frequency from 0 to 6 Hz led to grain refinement in the weld region [73]. At the same time, an increase in pulse frequency helps achieve better penetration (refer to Section 3.4), but an increase in the hump at the center of the weld and a large undercut due to high arc pressure limits the use of pulse frequency to a range up to 5 Hz. High arc pressure is maintained during high pulse frequency welding due to the high peak current and the reduced interval between consecutive peak currents. This decrease in delay due to increased frequency also increases overlap between the ripples, resulting in finer ripples. Current pulsing not only affects the development of ripples but also affects the microstructural development. The dissimilar welds produced using conventional and pulsed-GTAW at different frequencies were used to observe the effect of pulse frequency and compare it with conventional welds.

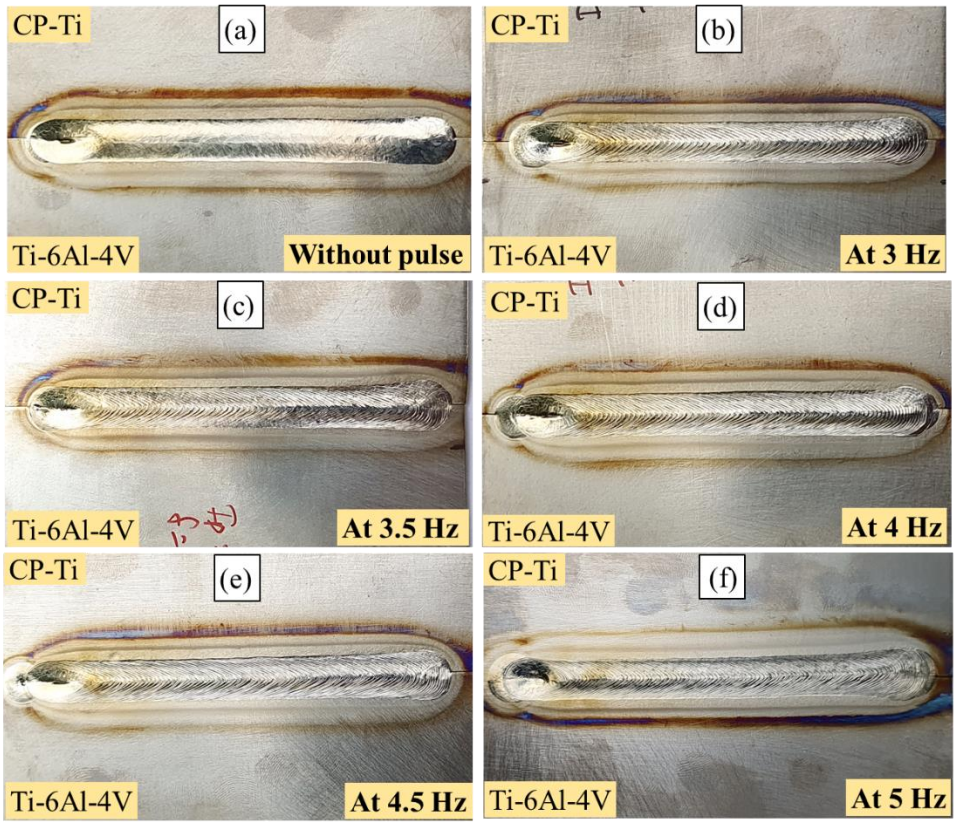

Figure 4.16 Dissimilar titanium alloy weld prepared using (a) Conventional GTAW; (b) at 3 Hz pulsed-GTAW; (c) at 3.5 Hz pulsed-GTAW; (d) at 4 Hz pulsed-GTAW; (e) at 4.5 Hz pulsed-GTAW; (f) at 5 Hz pulsed-GTAW

4.4.2 X-ray radiographic analysis dissimilar weld

X-ray radiography is a well-accepted non-destructive technique for assessing subsurface defects in welded parts. GTAW of titanium alloys is prone to tungsten inclusion, porosity, and oxide trapping in the welds. These impurities affect weld quality and deteriorate weld strength. Figure 4.17 (a-b) shows the X-ray radiographic films of dissimilar welded titanium alloys using conventional GTAW and pulsed GTAW at 4 Hz. In the radiographic films, no contrast difference was observed between CP-Ti and Ti-6Al-4V alloys. A significant difference between both films was observed in the weld region of the weldment. A broad and diffuse weld bead was observed for the conventional GTAW weld, while a narrow and bright weld bead was observed for the pulsed GTAW weld. Perfectly flat square butt edges were prepared, resulting in a very sharp hairline in the unwelded region of the butting-

edge, but no noticeable gap appeared between the edges. Both welds passed the X-ray radiography test and were free from any kind of subsurface defects. Similarly, other weldments were also tested, and similar results were observed between conventional GTAW and pulsed GTAW. All the weldments used in the study passed the radiographic tests and were free from any kind of subsurface defects.

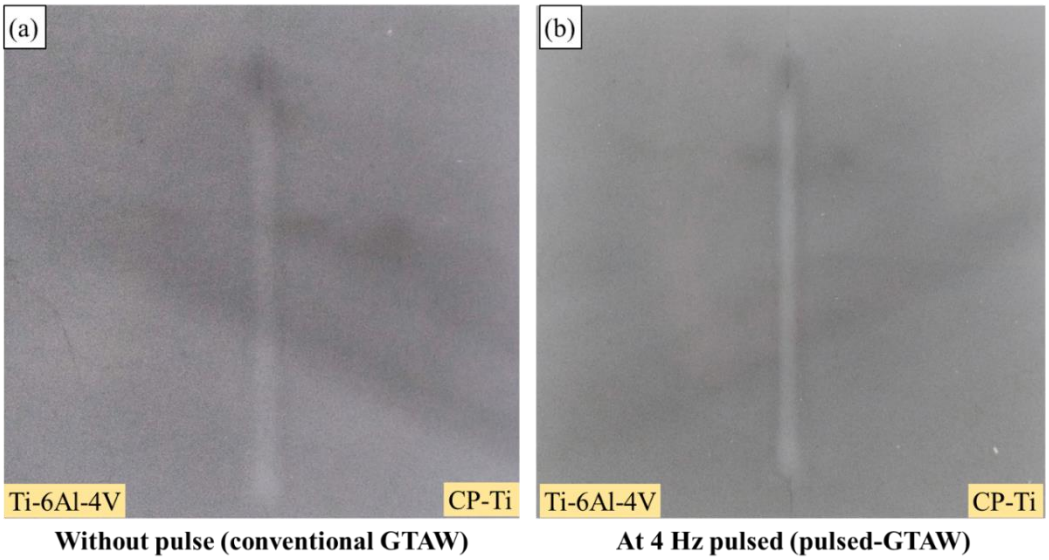

Figure 4.17 X-ray radiographic film of dissimilar (CP-Ti/Ti-6Al-4V) welded sheets: (a) using conventional-GTAW; (b) using p-GTAW at 4 Hz

4.4.3 Bead profile appearance at different pulse frequencies

As we observed in the last section, current pulsing during GTAW helps achieve steeper welds compared to conventional welds. A similar effect was obtained with dissimilar welds, where a broader, less steep weld bead profile was observed with conventional GTAW compared to pulsed GTAW. Figure 4.18 shows the dissimilar weld bead profiles obtained with conventional GTAW and pulsed GTAW at frequencies from 3 Hz to 5 Hz with intervals of 0.5 Hz. Due to the very intense heat source, equal melting was observed on either side of the weld despite the thermal conductivity difference between the two alloys. The weld parameters were set to ensure that the back width and front height fell within permissible limits, resulting in

a good quality weld. Along with variation in weld bead profile, current pulsing helped achieve full penetration at low heat input, resulting in a narrower HAZ on both the CP-Ti and Ti-6Al-4V sides compared to conventional GTAW. The HAZ width was at its maximum toward CP-Ti (3.81 mm) and Ti-6Al-4V (2.79 mm) with conventional GTAW. However, it decreased with increasing frequency, reaching 3.47 mm toward CP-Ti and 2.60 mm toward Ti-6Al-4V at 5 Hz pulsed GTAW welds. A similar trend was observed for weld bead width and weld area. The maximum weld bead width (8.05 mm) and weld area (11.50 mm²) were noted for conventional GTAW, while the minimum weld width (7.90 mm) and weld area (10.65 mm²) were observed for 5 Hz pulsed GTAW. Full-depth penetration was observed in all the welds without any noticeable defects.

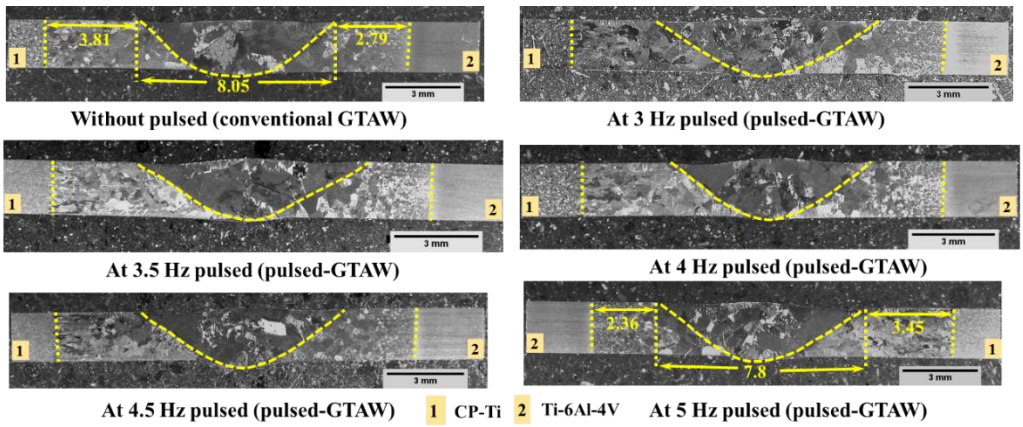

Figure 4.18 Dissimilar welded titanium alloy weld bead profiles using conventional and pulsed-GTAW at different frequencies

4.4.4 Microstructure evolution

Microstructure evolution was studied by extracting samples from different weld regions. The microstructure of the base material, HAZ, and the weld zone of the dissimilar weld produced autogenously using conventional-GTAW and pulsed-GTAW at different frequencies were observed at different magnifications and discussed.

4.4.4.1 Microstructure of base materials

The microstructure of as-received CP-Ti and Ti-6Al-4V materials has already been discussed in detail in Section 4.1.2 and Section 4.2.3. Figure 4.19 (a) shows the microstructure of as-received CP-Ti, a single-phase α-alloy with an equiaxed microstructure. Figure 4.19 (b) shows the bimodal microstructure of Ti-6Al-4V, where very fine grains of the dual-phase (α+β) alloy with bright and dark contrast are visible. The bright α-phase was uniformly distributed within a matrix of dark β-phase. These base metal microstructures were captured at the same magnification for comparison of grain size in the as-received condition.

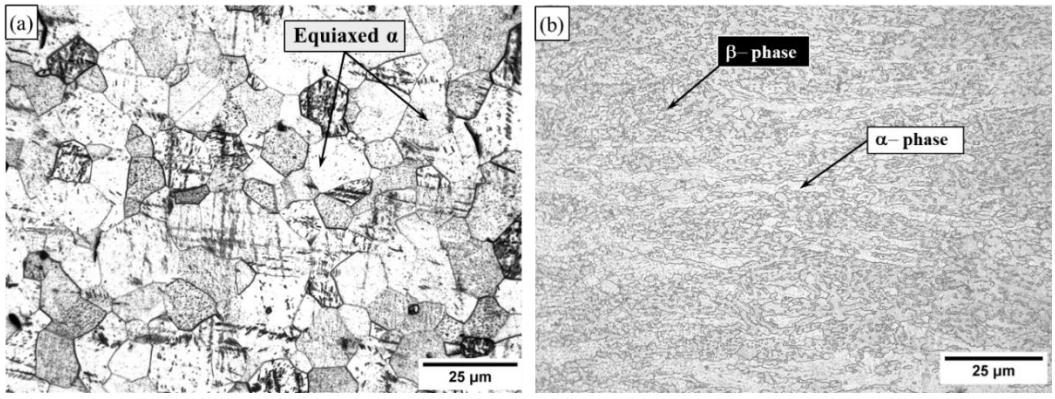

Figure 4.19 Microstructure of as-received material: (a) CP-Ti; (b) Ti-6Al-4V

4.4.4.2 Microstructure of heat affected zone (HAZ) at different frequencies

The microstructure of the HAZ appears due to the weld thermal cycle, and a gradual variation in the microstructure of the HAZ occurs due to variations in different temperatures reached and temperature gradients across the HAZ. Due to the three-dimensional (3-D) or mixed heat flow in conventional GTAW as well as in pulsed GTAW, the microstructure emerges in different regions with varying grain sizes and distributions [8]. In GTAW, mixed heat flow refers to heat distribution where the energy is more diffused and spread over a larger area due to the relatively broader arc, compared to high-energy beam welding processes like LBW and EBW. The heat

intensity in the GTAW process is lower, leading to a larger volume of material being affected, the development of a wider heat-affected zone (HAZ), and slower cooling rates. Due to the high heat input in GTAW and the low thermal conductivity of titanium alloys, heat could not dissipate rapidly from the weld region, resulting in grain coarsening in both the HAZ and the weld zone [3]. The data collected from the literature indicates that these if titanium alloys exceed the β-transus temperature, and the cooling rate is less than 100 °C/s, coarse prior-β grains will form. Since the cooling rate in the GTAW process is typically below 100 °C/s, grain coarsening in the prior-β grains occurs [29]. The appearance of prior-β grains indicates that the maximum temperature in the HAZ has exceeded the β-transus temperature, and grain coarsening suggests that this temperature persisted for a sufficiently long time. Figure 4.20 (a-f) shows the HAZ microstructure of the CP-Ti side of the dissimilar weld prepared using conventional-GTAW and pulsed-GTAW at pulse frequencies ranging from 3 Hz to 5 Hz with an interval of 0.5 Hz. The HAZ microstructure on the CP-Ti side of the dissimilar weld resembled that discussed for the case of bead-on-plate welding on CP-Ti in Section 4.2.3. However, refinement in prior-β grains was observed in the weld obtained using pulsed-GTAW compared to the weld obtained using conventional-GTAW, and this refinement increased with increasing pulse frequency. The refinement observed during current pulsing was due to the intermittent change in current level from peak to background and lower heat input. Further refinement with an increase in pulse frequency is attributed to the decrease in heat input and increased cooling rate. Prior-β grain refinement with an increase in pulse frequency was also observed by *Mehdi et al. (2016)* [64]. The absence of secondary phases in CP-Ti led to the development of large α-phase lamellae in the HAZ of CP-Ti. As discussed in the challenges of welding titanium alloys, grain

coarsening in both the heat-affected zone (HAZ) and the weld region is a major issue when using conventional welding processes like GTAW. However, current pulsing during GTAW aided in grain refinement in the HAZ on the CP-Ti side. This refinement improved further with increased pulse frequency, and the finer microstructure enhanced the mechanical properties were obtained.

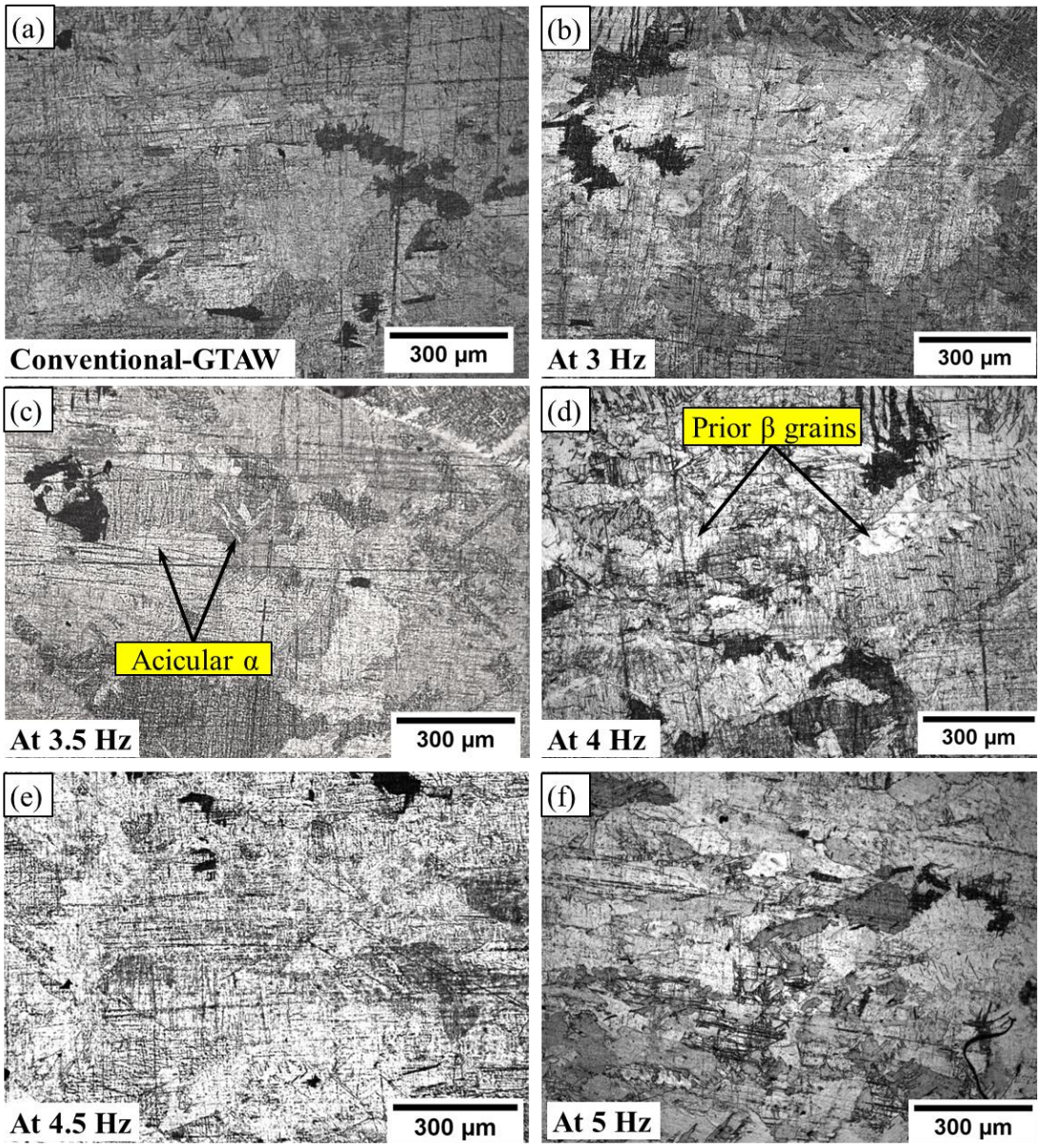

Figure 4.20 Microstructure of HAZ towards CP-Ti side: (a) using conventional-GTAW; (b) using pulse-GTAW at 3 Hz; (c) using pulse-GTAW at 3.5 Hz; (d) using pulse-GTAW at 4 Hz; (e) using pulse-GTAW at 4.5 Hz; (f) using pulse-GTAW at 5 Hz

Figure 4.21 (a-f) shows the HAZ microstructure of Ti-6Al-4V side of dissimilar weld prepared using conventional-GTAW and pulsed-GTAW at pulse frequencies from 3 Hz to 5 Hz with an interval of 0.5 Hz. The HAZ microstructure appeared towards Ti-6Al-4V side of the dissimilar weld, which was similar to what was discussed for the case of bead-on-plate welding on Ti-6Al-4V in Section 4.1.2. Similar to the current pulsing effect on HAZ of CP-Ti side grain refinement in prior-β grains were observed for the HAZ of Ti-6Al-4V, and prior-β grains were decreasing with increasing frequency. Although, the thermal conductivity of CP-Ti (20 W/m-k) is higher than that of Ti-6Al-4V (7 W/m-k), the absence of a secondary phase in CP-Ti results in severe unrestricted growth of prior-β grains in the HAZ; therefore, very diffused prior-β boundaries were observed. However, the presence of a secondary phase in Ti-6Al-4V helped overcome the effect of low thermal conductivity and produced a finer microstructure and sharper grain boundary were observed in the HAZ Ti-6Al-4V side. In both cases, due to comparatively faster cooling during welding, the fine acicular α-phase nucleated inside and at the prior β grain boundaries. The microstructure of HAZ on the Ti-6Al-4V side consists of retained α, acicular α and β-phase, whereas the microstructure of HAZ on the CP-Ti has retained α and acicular α inside the prior β-grains or appears independently. *Wang et al. (2006)* observed the retained α and β-phase inside the prior β grain in the microstructure of HAZ during dissimilar welding of Ti-6Al-4V and IMI834 titanium alloys [127]. GTAW welded samples usually have a cooling rate of less than 20 °C/s, and therefore, the possibility of martensite formation in HAZ and the weld zone is very low [29, 121]. The α-phase present in the HAZ of welded samples is in the form of acicular-α or α-lamellae, which contributes to strengthening the near-HAZ of either side.

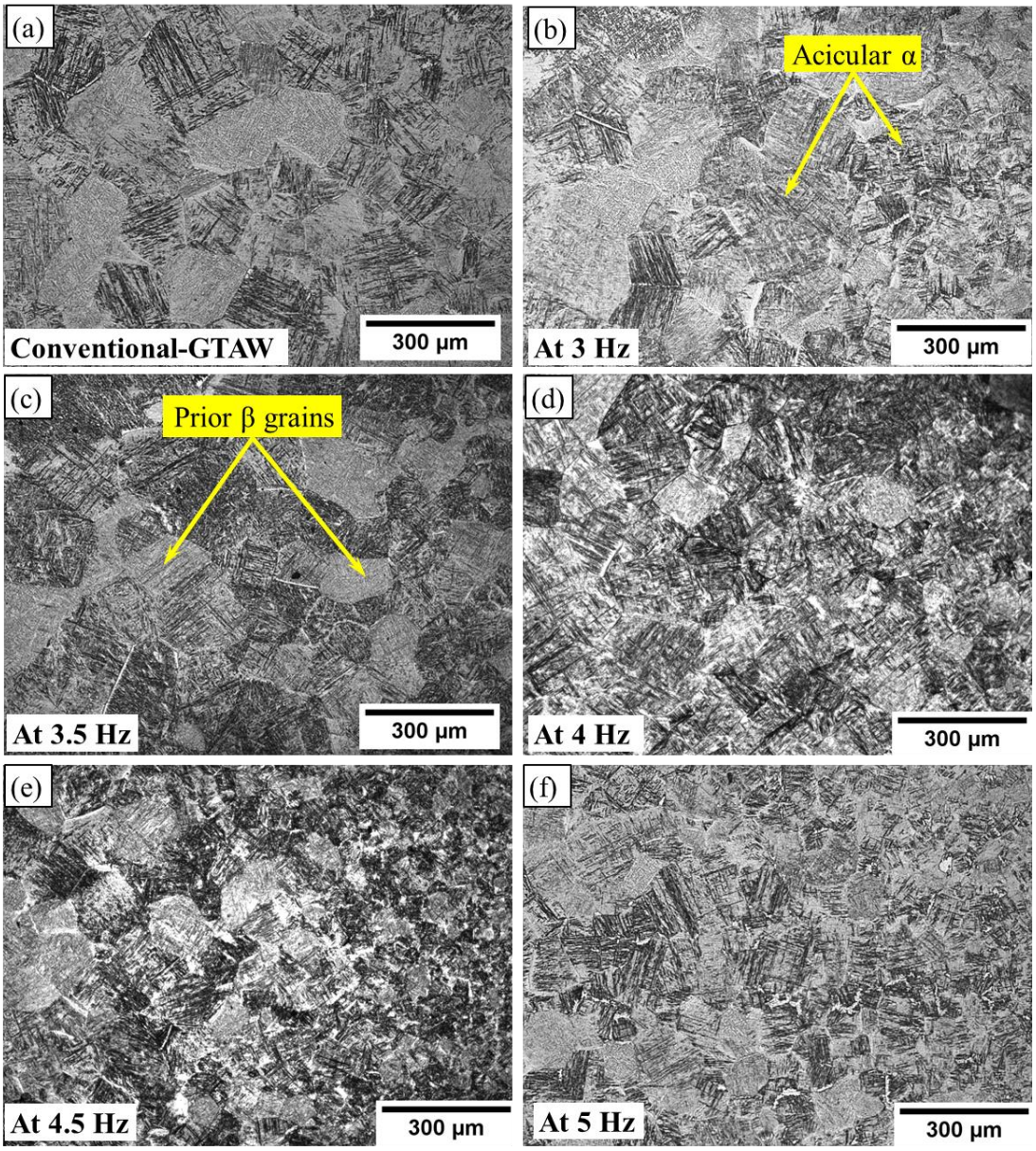

Figure 4.21 Microstructure of HAZ towards Ti-6Al-4V side: (a) using conventional-GTAW; (b) using pulse-GTAW at 3 Hz; (c) using pulse-GTAW at 3.5 Hz; (d) using pulse-GTAW at 4 Hz; (e) using pulse-GTAW at 4.5 Hz; (f) using pulse-GTAW at 5 Hz

4.4.4.3 Microstructure of dissimilar weld zone at different frequencies

Severe grain coarsening of prior-β grains usually appears in the weld and HAZ regions, and it grows up to a few millimeters. Sometimes, it became difficult to capture the entire grain or observe the prior-β grain boundaries in the micrographs at higher magnifications. Figure 4.22 (a-f) shows the microstructure of the weld region

of dissimilar weld prepared using conventional-GTAW and pulsed-GTAW at pulse frequencies from 3 Hz to 5 Hz with an interval of 0.5 Hz. The prior-β grains in the weld region were randomly distributed, and a complex microstructure was observed. Similar to the microstructures observed and discussed for bead on plate welding on CP-Ti and Ti-6Al-4V in Sections 4.1.2 and 4.2.3, grain coarsening was observed in the weld and HAZ region of the dissimilar weld. However, the average grain size of prior-β grains was maximum (~320 μm) for the weld prepared using conventional-GTAW, and it was decreasing with increasing the pulse frequency. A minimum (~180 μm) average grain size of prior-β grains was observed for the weld prepared using 5 Hz pulsed frequency. Because of the large prior-β grains, these microstructures were captured at low magnification; therefore, most of the microfeatures were not resolved at this magnification. These micro-features appeared near the grain boundary or inside the grain boundary as dark regions.

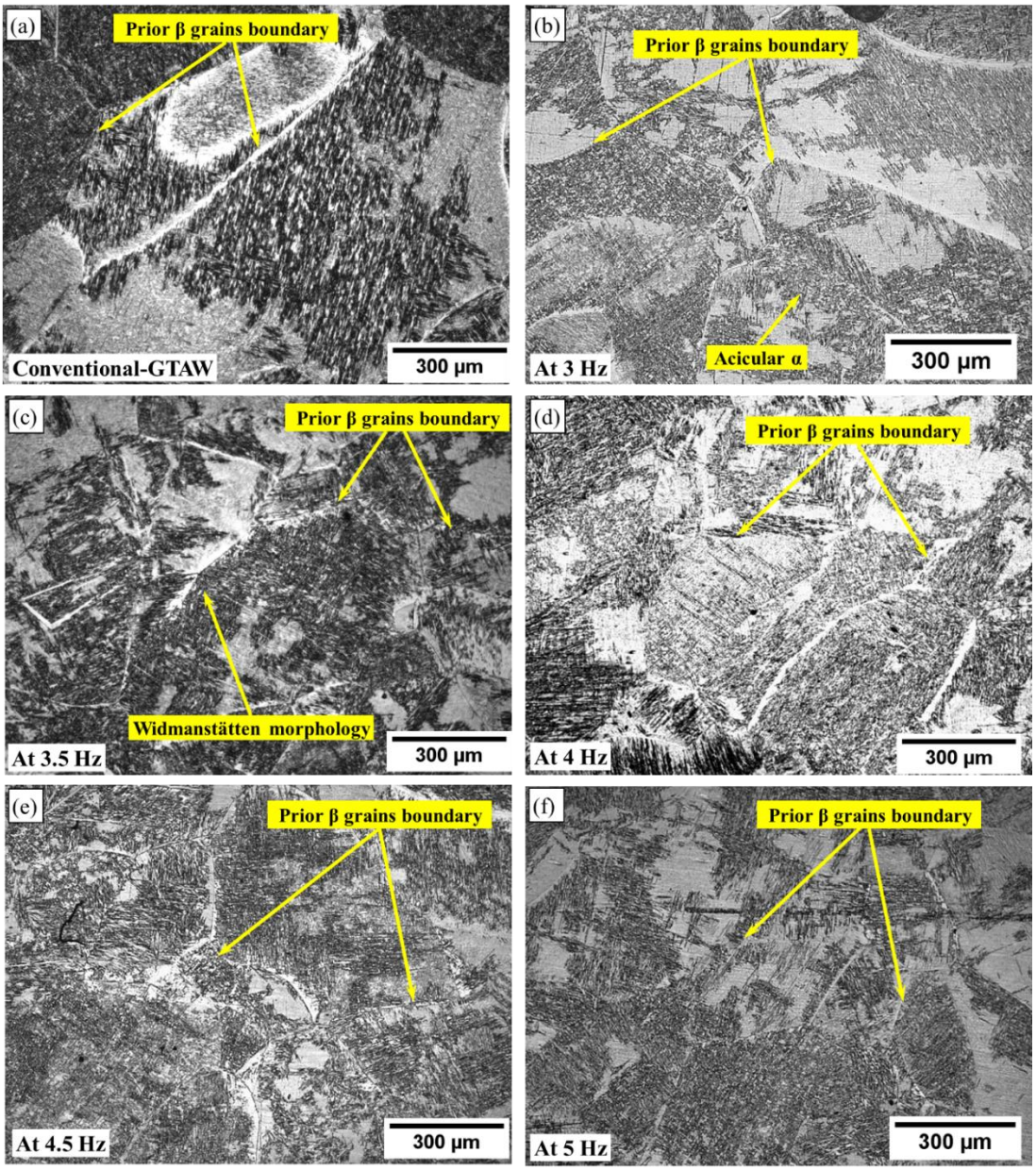

Figure 4.22 Microstructure of the weld region of dissimilar weld: (a) using conventional-GTAW; (b) using pulse-GTAW at 3 Hz; (c) using pulse-GTAW at 3.5 Hz; (d) using pulse-GTAW at 4 Hz; (e) using pulse-GTAW at 4.5 Hz; (f) using pulse-GTAW at 5 Hz

To resolve the dark regions in the weld microstructures that appeared at low magnification, the microstructures were observed at high magnifications. Figure 4.23 (a) shows the microstructure of the dissimilar weld region at 50x, highlighting the dark region, which was resolved at high magnifications (100x, 200x, and 500x) in Figure 4.23 (b-d) to observe the microfeatures that appeared near the grain boundaries and inside the prior β-grains. When these microstructures were observed

at high magnifications, the dark regions near the grain boundaries were mostly in Widmanstätten morphology, which nucleated from the prior β-grain boundaries, while the dark regions inside the prior-β grains consisted of acicular α-phase, α-phase laths, and basketweave morphology surrounded by β-phase. *Wang et al. (2011)* observed that the secondary phase present in the material restricts the grain growth of another phase [128]. Here also, the retained β-phase restricted the grain growth of α-phase inside the prior β grains; therefore, a refined microstructure was observed inside the prior-β grains of the dissimilar weld compared to the weld zone of the single-phase CP-Ti weld in Section 4.2.3. Similar results were observed with conventional-GTAW and pulsed-GTAW at each frequency, with little variation in morphology. Finer acicular-α and Widmanstätten morphology were observed with pulsed-GTAW welds at high frequencies compared to conventional-GTAW welds.

The formation of internal features within prior-β grains is a common phenomenon; however, these features were also influenced by the application of pulse frequency, leading to further refinement. The mechanical properties of dissimilar welds depend on both prior-β grain size and morphology observed in the microstructure. This refinement of internal features contributed to the improvement of the high-temperature strength of the weldment. The effect of prior-β grain size and morphology observed in the weld region has been discussed in detail in the mechanical testing section.

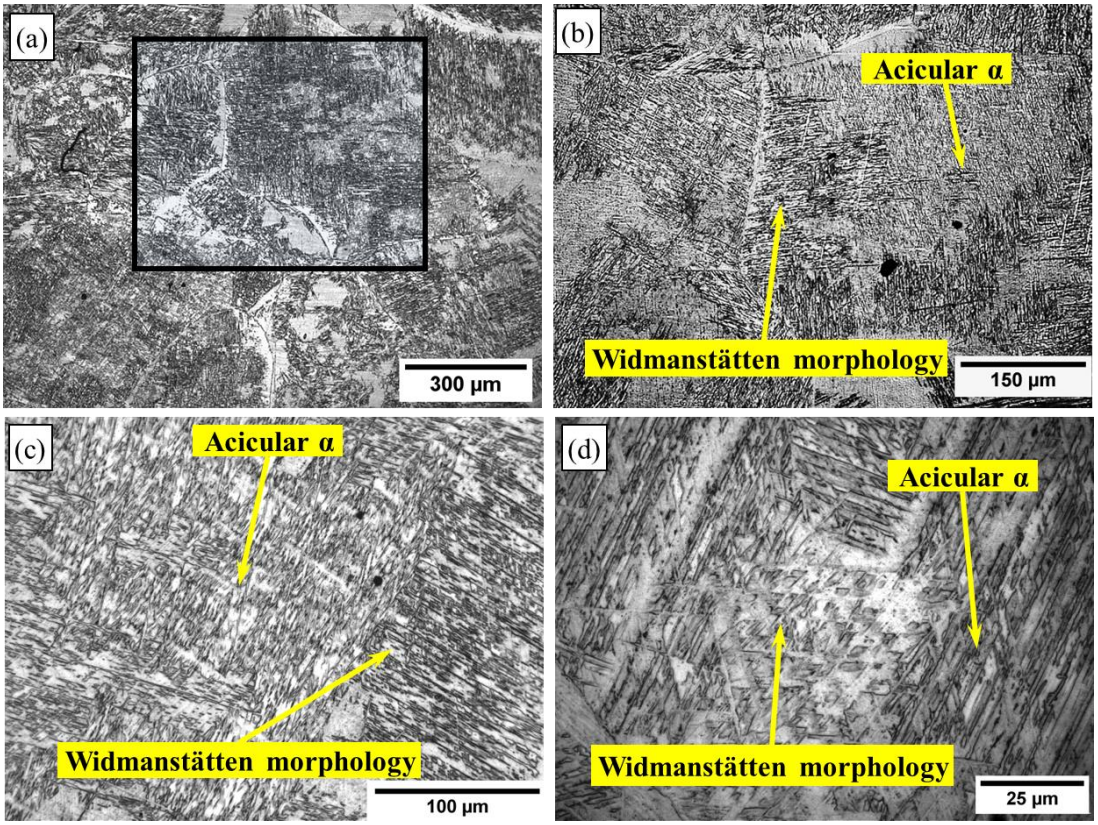

Figure 4.23 Microstructure of weld region at different magnification; (a) at 50x; (b) at 100x; (c) at 200x; (d) at 500x

4.4.5 EDS analysis of weld region of dissimilar weld

The variation of solute particles in the weld region of dissimilar weld produced using conventional-GTAW and pulsed-GTAW at 5 Hz frequency was analysed using energy dispersive X-ray spectroscopy (EDS) at different locations of the welds. The pulsed-GTAW at 5 Hz was selected to observe the maximum effect of current pulsing during welding. Figure 4.24 shows the EDS spectrum of dissimilar weld produced using conventional-GTAW at different locations of the weld. EDS was performed at three locations of the weld zone, where two were at the extremities of the weld region, i.e., near the fusion boundary of Ti-6Al-4V and the CP-Ti side, and one was performed at the center of the weld. These locations are also indicated in the inset of the figure. Figure 4.24 (a) shows the EDS spectrum near the fusion boundary of the Ti-6Al-4V side; Figure 4.24 (b) shows the EDS spectrum at the center, and Figure 4.24 (c) shows the EDS spectrum near the fusion boundary of CP-Ti. The EDS

elemental analysis of dissimilar weld produced using conventional-GTAW confirmed that the wt.% of ‘Al’ and ‘V’ varied throughout the weld region. This non-uniform mixing occurs near the fusion boundary due to rapid cooling and solidification during welding. *Wang et al. (2016)* also observed non uniform mixing during dissimilar welding of titanium alloys [127]. The wt.% of ‘Al’ varied from 3.50 to 2.90, and the wt.% of ‘V’ varied from 1.93 to 0.19 from the fusion boundary towards the Ti-6Al-4V side to the fusion boundary towards the CP-Ti side. The lightweight ‘Al’ exhibited superior mobility and was distributed almost uniformly throughout the weld; however, ‘V’ is relatively heavier and appears to be less mobile. The variation of the β-phase stabilizer (wt.% of ‘V’) throughout the weld led to variations in the amount of β-phase that appeared across the weld.

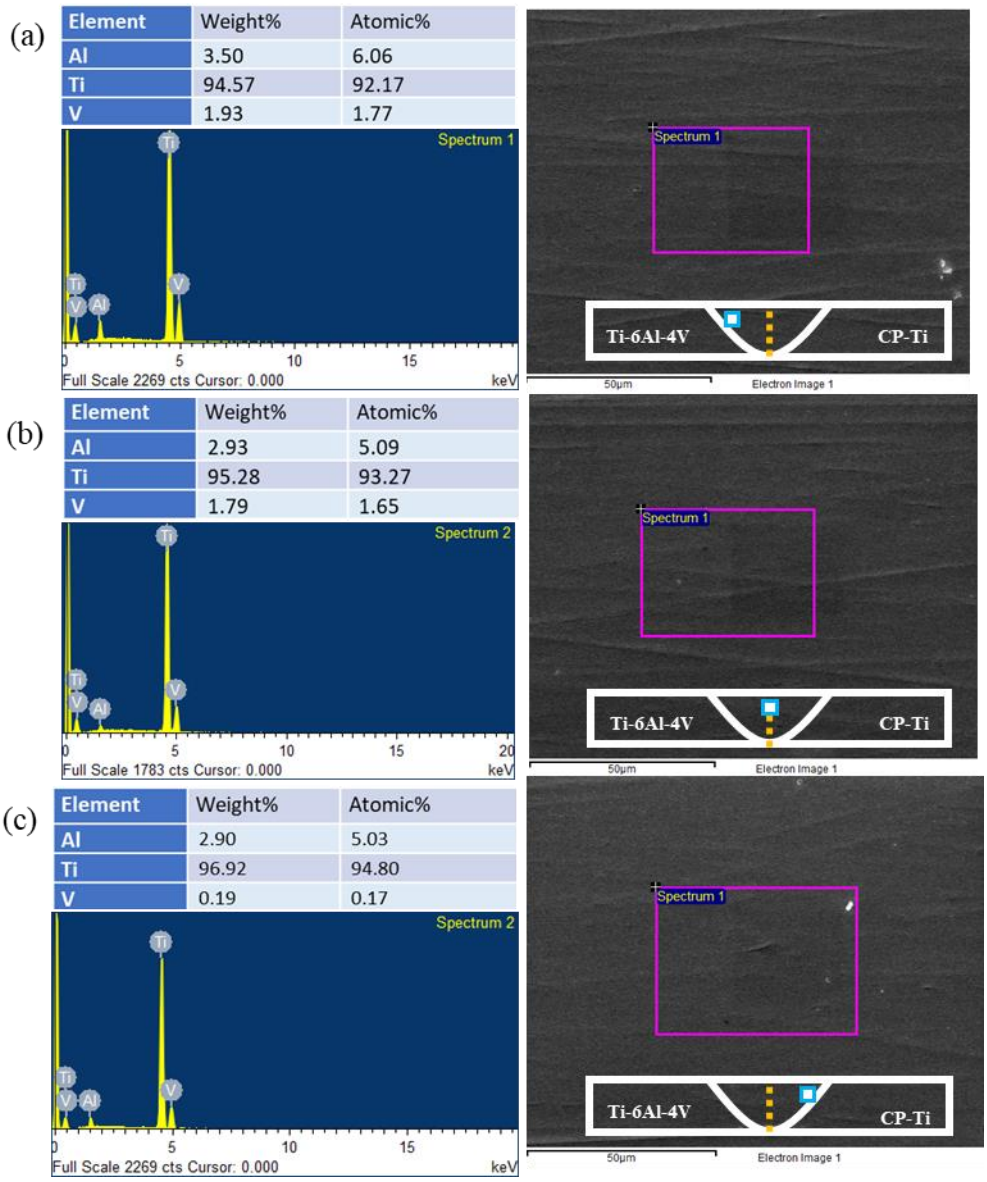

Figure 4.24 EDS spectrum analysis of dissimilar weld produced using conventional-GTAW at different location of the weld: (a) near fusion boundary of Ti-6Al-4V; (b) at the center of the weld; (c) near fusion boundary of CP-Ti side

Figure 4.25 shows the EDS spectrum of dissimilar weld produced using pulsed-GTAW at different locations of the weld. Similar to conventional-GTAW weld, EDS was performed near the fusion boundary of Ti-6Al-4V and the CP-Ti side and at the center of dissimilar weld. Figure 4.25 (a) shows the EDS spectrum near the fusion boundary of Ti-6Al-4V side, Figure 4.25 (b) shows the EDS spectrum at the center, and Figure 4.25 (c) shows the EDS spectrum near the fusion boundary of CP-Ti. Similar to conventional-GTAW weld, the wt.% of 'Al' and 'V' varied throughout the

weld region of pulsed-GTAW dissimilar weld. The wt.% of ‘Al’ varied from 3.74 to 3.44, and the wt.% of ‘V’ varied from 1.66 to 0.99 from the fusion boundary towards Ti-6Al-4V side to the fusion boundary towards CP-Ti side. Similar to conventional-GTAW weld, ‘Al’ showed high mobility and was almost uniformly distributed throughout the weld. The major alloying elements in Ti-6Al-4V are aluminum and vanadium. During welding of this alloy (and welding of dissimilar alloys), aluminum was found to distribute uniformly even without pulsing. This may be due to aluminum's higher diffusivity in titanium compared to vanadium, as well as the similar atomic radii of aluminum and titanium. In contrast, vanadium has a lower diffusion rate in titanium and does not mix uniformly during conventional GTAW. However, pulsed GTAW increased arc stirring, leading to more uniform mixing of vanadium in the weld. Because of the variation in β-stabilizers throughout the weld, the amount of β-phase also varied across the weld region, resulting in variations in the mechanical properties throughout the weld. This variation of the β-phase also altered the grain size throughout the weld zone, and larger grain coarsening was observed towards the CP-Ti side.

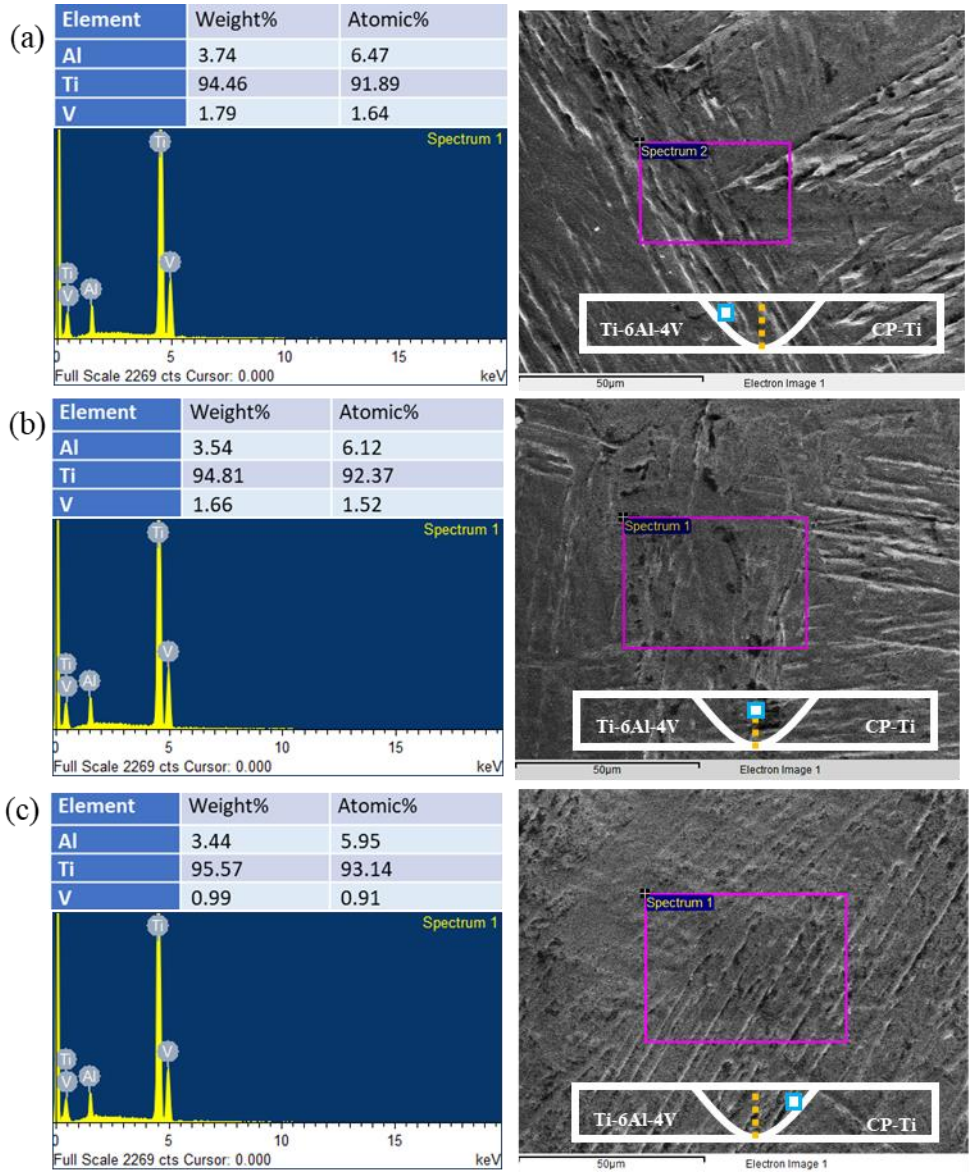

Figure 4.25 EDS spectrum analysis of dissimilar weld produced using pulsed-GTAW at different location of the weld: (a) near fusion boundary of Ti-6Al-4V; (b) at the center of the weld; (c) near fusion boundary of CP-Ti side

4.4.6 X-ray diffraction analysis of as-received materials and dissimilar welds

Samples for X-ray diffraction (XRD) was extracted from as-received materials and welded regions of welds produced using conventional-GTAW and pulsed-GTAW at 5 Hz. Figure 4.26 (a-d) shows the XRD profiles obtained for as-received CP-Ti, as-received Ti-6Al-4V, and weld zones of dissimilar weld produced using conventional-GTAW and pulsed-GTAW respectively. To identify the phases present in the as-received materials and dissimilar welds, X-rays were irradiated, and intensity vs. 2θ

plots were drawn. X'Pert HighScore Plus software was utilized to analyze and match XRD peaks. Figure 4.26 (a) shows the XRD profile of CP-Ti, where all the major peaks were matched with the hexagonal close-packed (hcp) structure of titanium alloys, i.e., with pure titanium or the α-phase of titanium alloys. However, Figures 4.26 (b-d) show the XRD profiles for Ti-6Al-4V and both the welds, where the peaks corresponding to (011) and (112) planes appeared in shoulder form, confirming the presence of the β-phase in the as-received Ti-6Al-4V and the weld zones of both welds. The prominent peaks of as-received CP-Ti were matched with reference code 98-007-6144, and the peaks of Ti-6Al-4V and of dissimilar weld zones were matched with reference codes 98-007-6165 and 98-007-6254, respectively. There were no peaks in the weld area owing to the presence of any oxides or any new phases. The major peak intensities in the weld region decreased from the as-received Ti-6Al-4V. The peak intensities depend on amount of phases and the morphology present in the material, and a reduction in peak intensities indicates the conversion of fine globular or equiaxed morphology of α-phase to large plate-like and needle-like morphology [129]. This conversion was also evident in the microstructural change in the weld region of dissimilar weld from the as-received Ti-6Al-4V, where the morphology of the weld region was converted into large plate-like alpha and fine acicular alpha from equiaxed morphology of base Ti-6Al-4V (Section 4.4.4.1). The prominent α peak of CP-Ti was strongest and its intensity diminished for other samples, i.e., the amount of α-phase was decreased in other cases, similar trend was observed and correlated with the optical micrographs.

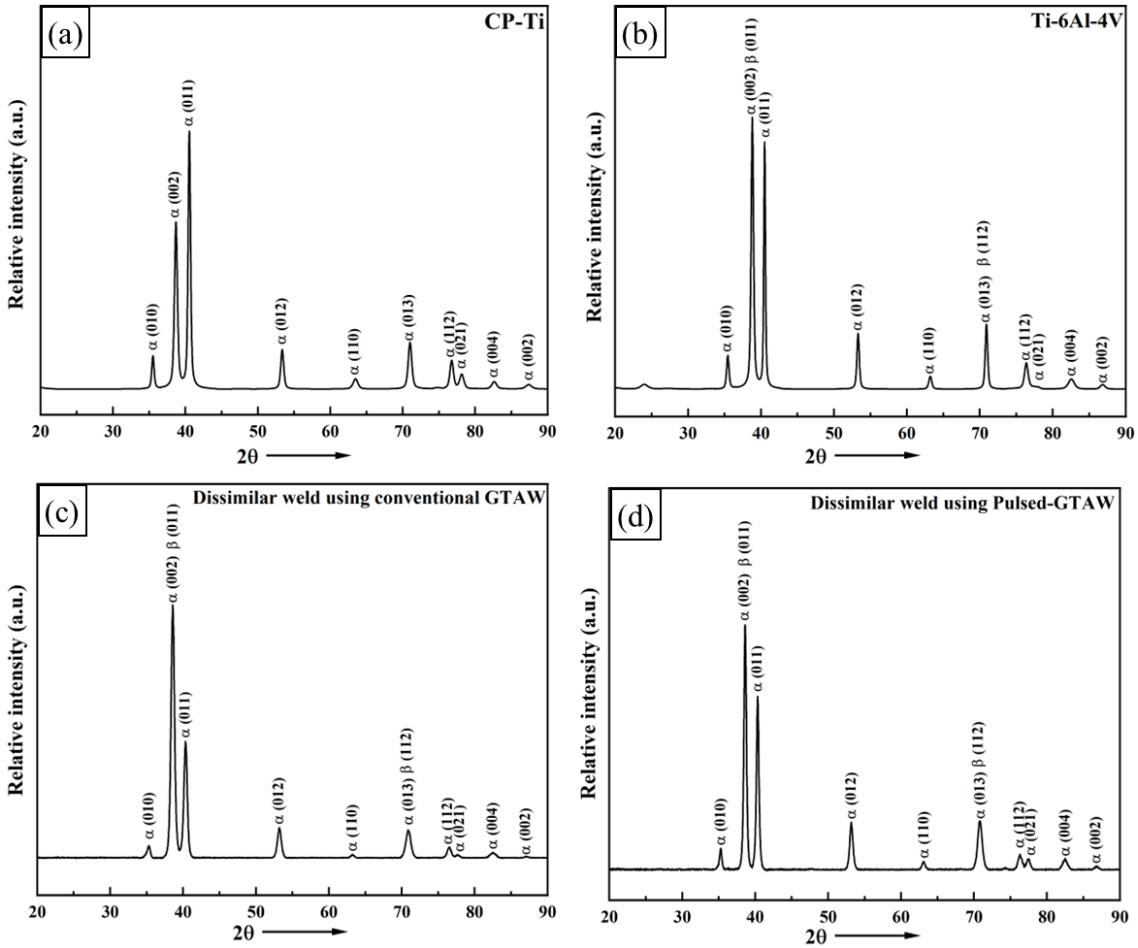

Figure 4.26 XRD pattern of: (a) CP-Ti; (b) Ti-6Al-4V; (c) dissimilar weld using conventional-GTAW; (d) Dissimilar weld using pulsed-GTAW

4.4.7 Mechanical testing

Mechanical testing of welded joints involves assessing properties like tensile strength, toughness, and hardness to evaluate weld integrity. Various techniques, including tensile testing, impact testing, and microhardness testing, are employed to analyze weld performance under different loading conditions ensuring structural reliability and safety.

4.4.7.1 Microhardness variation across the dissimilar weld

Microhardness measurement was done across the weldment, i.e., from the CP-Ti base material to the Ti-6Al-4V base material. The indentation for microhardness measurements was made as per the scheme discussed in Section 3.8.5, where

indentations were made at an interval of 1 mm, and three indentations were made at particular locations by moving the indenter in the thickness direction. Figure 4.27 (a) shows the microhardness variation across the weldment of conventional-GTAW weld and pulsed-GTAW welds at 3, 3.5, 4, 4.5 and 5 Hz frequencies. To analyze the microhardness variation throughout the weld, the average Vickers hardness number (HV) of three indentations has been plotted with respect to their locations. Due to the difference in mechanical properties, including the hardness of CP-Ti and Ti-6Al-4V alloys, an asymmetry in microhardness was observed in the weldment. CP-Ti is having much lower hardness than Ti-6Al-4V alloy, therefore, the microhardness in the weldment increased from the CP-Ti side to the Ti-6Al-4V side in both weldments. A very little variation was observed in the microhardness of single phase as-received CP-Ti; however, due to the presence of different phases and variations in grain sizes, variation in microhardness was observed in the as-received Ti-6Al-4V alloy. The hardness obtained in the base metal and HAZ of CP-Ti were nearly the same; however, a dip in hardness was observed in the far-HAZ of Ti-6Al-4V side, due to grain coarsening and the absence of acicular-α morphology in this region. In spite of grain growth of prior β in HAZ of CP-Ti, this has not resulted in the corresponding decrease in the hardness because of the subsequent formation of acicular α upon cooling. The microhardness variation was also observed in the weld region of dissimilar weld due to variation in microstructure and amount of β-phase (driven by the β-phase stabilizer) across the weld region, which was also evident from the EDS results from the different regions of the weld zone. A similar trend was observed for variation in microhardness across the weldment prepared using conventional-GTAW or pulsed-GTAW at any frequency tested. For observing the effect of current pulsing on the hardness of the weldment, the microhardness was

plotted with respect to location across the weldment of conventional-GTAW weld and pulsed-GTAW weld at 5 Hz frequency, as shown in Figure 4.27 (b). The increased hardness was obtained in the HAZ, and the weld region of dissimilar weld produced using pulsed-GTAW at 5 Hz. This improvement in hardness in pulsed-GTAW weld can be corelated with the refinement observed in the microstructure in the HAZ and weld-zone using pulsed-GTAW [29]. The current pulsation helped in increase in hardness; however, the increase was not significant. It should also be noted that the current pulsing did not lead to the formation of any new hard phase after welding even at different frequencies. Therefore, very little difference in hardness was observed at different frequencies which was caused due to grain refinement. Maximum average hardness (~342 $HV_{0.2}$) was obtained beyond the HAZ in the base metal of Ti-6Al-4V, and average hardness in the base metal of CP-Ti was obtained as 135 $HV_{0.2}$.

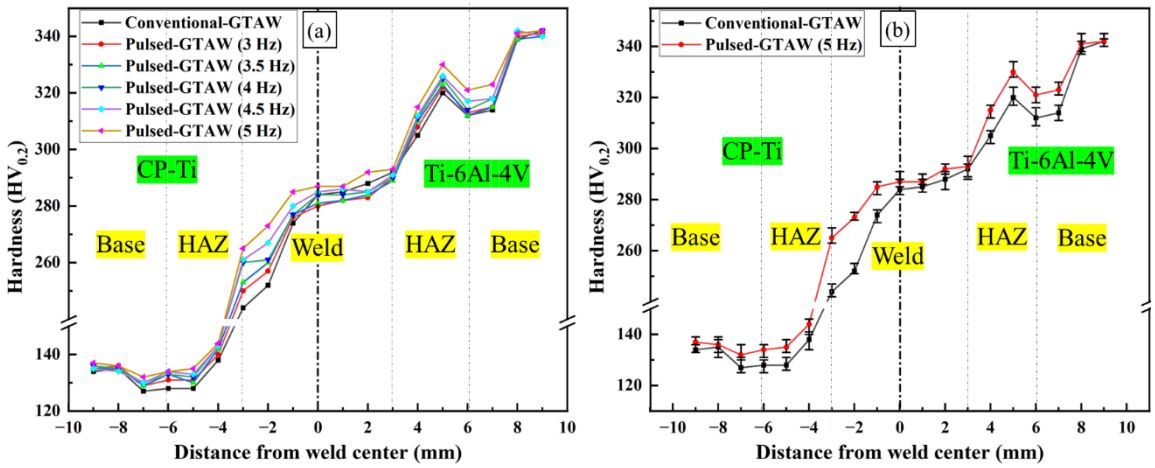

Figure 4.27 (a) Microhardness variation across the weldment of conventional-GTAW weld and pulsed-GTAW welds at 3, 3.5, 4, 4.5 and 5 Hz frequencies; (b) microhardness variation across the weldment of conventional-GTAW weld and pulsed-GTAW welds at 5 Hz frequencies

Figure 4.28 shows the average microhardness in the HAZ of CP-Ti side, HAZ of Ti-6Al-4V side, and the weld region of dissimilar produced using conventional-GTAW (UP) welds and pulsed-GTAW welds at 3, 3.5, 4, 4.5, and 5 Hz frequencies. An

increase in pulse frequency during pulsed-GTAW helps in grain refinement in the HAZ and weld region of dissimilar welds, which is also evident from the increased hardness with increasing frequency. The average hardness in the HAZ of CP-Ti side increased from 127 $HV_{0.2}$ to 133 $HV_{0.2}$, the average hardness in the HAZ of the Ti-6Al-4V side increased from 312 $HV_{0.2}$ to 322 $HV_{0.2}$, and the hardness in the weld center increased from 281 $HV_{0.2}$ to 286 $HV_{0.2}$ for the weld prepared using conventional-GTAW and pulsed-GTAW at a frequency of 5 Hz. This improvement in hardness using pulsed-GTAW helps to improve the strength of the weld joint. The developed shielding set-up helped in obtaining the hardness values within the acceptable limits, and no abnormal spikes of hardness appeared in any portion of the weld. Any excessively high hardness in any region of the weldment may deteriorate the toughness of the weldment [35]. Weldment with moderate hardness possesses sufficiently good ductility and toughness [111].

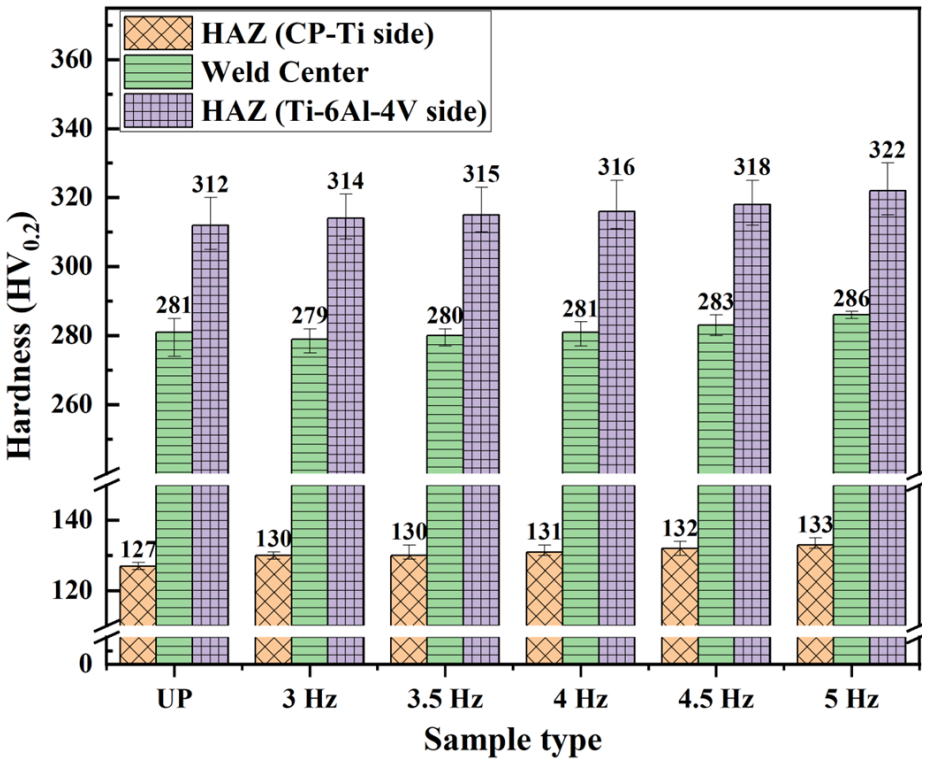

Figure 4.28 Average microhardness of the HAZ (CP-Ti side), HAZ (Ti-6Al-4V side) and dissimilar weld region produced using conventional-GTAW (UP) weld and pulsed-GTAW welds at 3, 3.5, 4, 4.5 and 5 Hz frequency

4.4.7.2 Tensile testing of as-received CP-Ti and Ti-6Al-4V and dissimilar weld specimens

Two types of tensile specimens were tested to study the strength of the welded dissimilar weld samples and compare them to the as-received CP-Ti and Ti-6Al-4V alloys. These specimens were prepared and tested as per the procedure discussed in Section 3.8.6.

Reduced-section tensile testing

Reduced-section tensile specimens were prepared to assess the strength of the weld joint. Figure 4.29 (a) shows the polished, non-standard reduced-section tensile specimens. These specimens were extracted from the as-received CP-Ti and Ti-6Al-4V alloy, as well as dissimilar welded samples using conventional-GTAW and pulsed-GTAW at pulse frequencies ranging from 3 Hz to 5 Hz with an interval of 0.5 Hz. The stress-strain relationship for reduced-section specimens differs from that of full-length standard tensile specimens due to stress concentration. The cross-section of these specimens was reduced at the weld section and in the middle of as-received specimens. Three specimens were tested under each condition for repeatability of results at room temperature and the same strain rate, and all the tested specimens followed the same trend. Figure 4.29 (b) shows the reduced-section specimen mounted on the universal testing machine (UTM), and Figure 4.29 (c) shows the tested and broken reduced-section tensile specimens. All tensile testing specimens were fractured in the gauge section, with base material specimens fractured from the middle of the gauge section, whereas all the dissimilar welded specimens were fractured away from the weld center and near the HAZ/fusion boundary of the CP-Ti side. Increasing the pulse frequency during GTAW from conventional-GTAW shifted the point of fracture towards the weld center from the HAZ/fusion boundary.

This shift in the point of fracture can also be observed in the fractured samples in Figure 4.29 (c), where the point of fracture in conventional-GTAW weld and pulsed-GTAW weld at 5 Hz frequency has been highlighted, showing a clear shift in the point of fracture. The stress-strain relationship for reduced-section tensile specimens of base material and welded specimens is shown in Figure 4.29 (d).

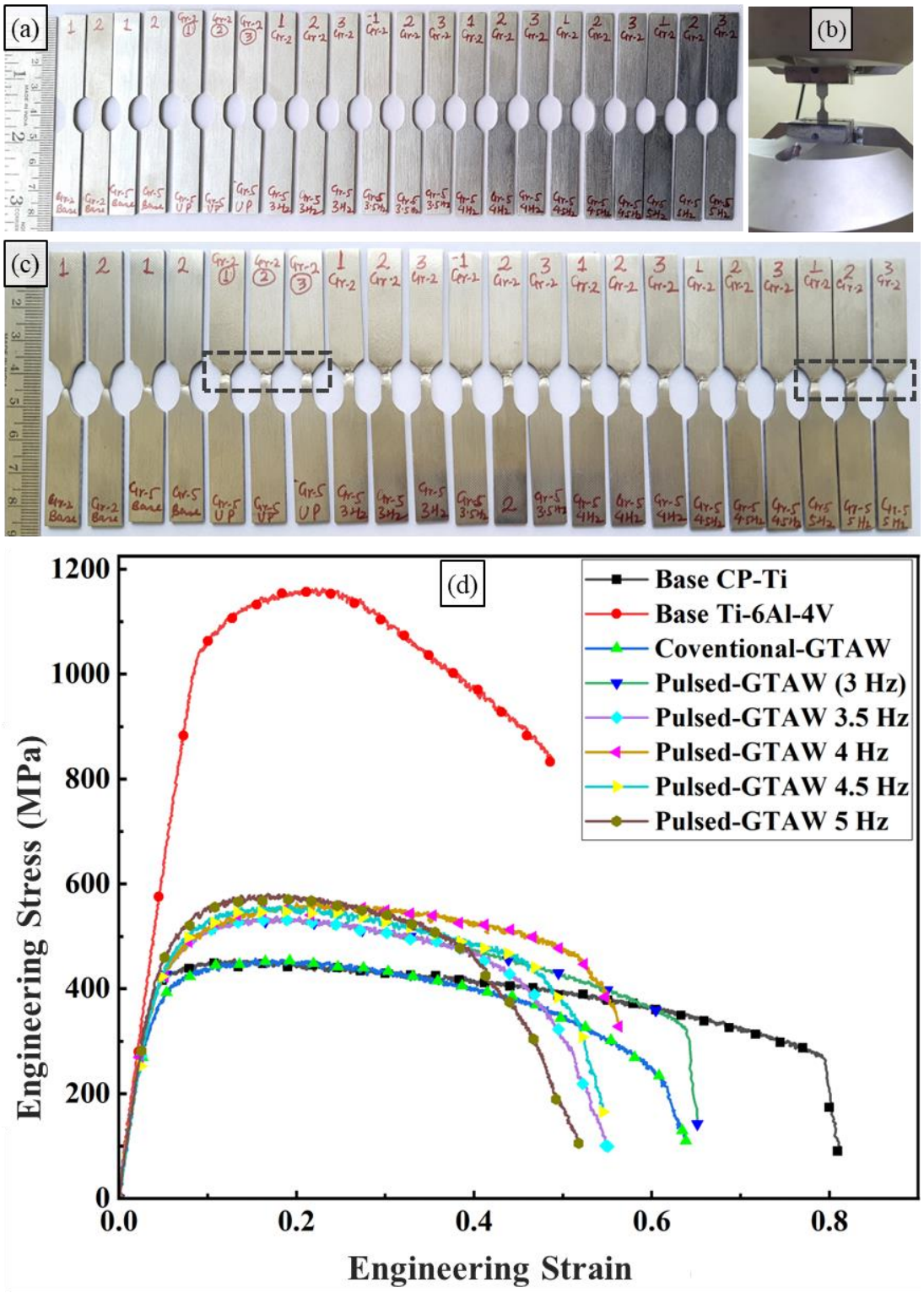

Figure 4.29 (a) Reduce-section tensile test specimens; (b) sample mounted on UTM; (c) fractured reduced-section tensile specimens; (d) stress-strain diagram for reduced-section tensile test specimen

The yield strength at 0.2% offset and ultimate tensile strength (UTS) obtained for the reduce-section tensile specimens are listed in Table 4.4. The base material Ti-6Al-4V

stood strongest among all the specimens and showed maximum yield strength (1050 MPa) and UTS (1157 MPa). The yield strength and UTS of the welded specimens were increasing with increasing pulse frequency. The yield strength of base CP-Ti (365 MPa) lied in between the welded specimens; however, the UTS of all welded specimens was higher than that of base CP-Ti (UTS 450), i.e., the weld prepared at any condition was stronger than the weakest material of dissimilar weld. The yield strength (380 MPa) and UTS (570 MPa) were found at maximum for pulse-GTAW weld at 5 Hz frequency, and minimum for conventional-GTAW weld (yield strength 265 MP and UTS 453 MPa). Much discussion cannot be made on elongation due to the non-standard tensile specimen, however, elongation was decreasing with increasing pulse frequency. This increase in UTS and decrease in elongation using pulse-GTAW at high frequency can be attributed to the formation of martensite (α') due to low heat input and a high cooling rate at a higher pulsed frequency [8, 29].

Table 4.5 Results obtained from reduced-section tensile specimens of dissimilar weld

Specimen	**Yield strength (At 0.2 % offset) [MPa]**	**Ultimate Tensile Strength [MPa]**
Ti-6Al-4V (as-received)	1050	1157
CP-Ti (as-received)	365	450
Using Conventional-GTAW	265	453
Pulsed-GTAW (3 Hz)	334	534
Pulsed-GTAW (3.5 Hz)	338	535
Pulsed-GTAW (4 Hz)	339	558
Pulsed-GTAW (4.5 Hz)	352	357
Pulsed-GTAW (5 Hz)	380	570

Figure 4.30 (a-d) shows the scanning electron microscope (SEM) micrographs of the fractured reduced-tensile specimens of as-received CP-Ti, as-received Ti-6Al-4V, and dissimilar welds produced using conventional-GTAW and pulsed-GTAW at 5 Hz, respectively. When these fractured specimens were analyzed under high-

resolution SEM, mostly intergranular fractures were observed in those specimens, and fractured surfaces appeared dull in all the specimens. The as-received CP-Ti and Ti-6Al-4V had almost equiaxed dimples; however, finer dimples were observed in the as-received Ti-6Al-4V. Both the as-received materials were fractured in ductile fashion, and ductile tears were clearly visible in micrographs. The dimples observed in the fractured sample of conventional-GTAW welds were coarser than the dimples observed in the pulsed-GTAW. This was also evident from the microstructure of pulsed-GTAW welds at 5 Hz, where grain refinement took place in pulsed-GTAW in comparison to conventional-GTAW. Welded specimens had variation in dimple size in the fractured region, and more facets were observed in pulsed-GTAW welds in comparison to the conventional-GTAW. The formation of a small amount of martensite in the weld region of pulsed-GTAW helped in improving strength of the weld and produced more cleavage facets in the weld region. The welded specimens were fractured in the weld region near the HAZ/fusion boundary of CP-Ti side, and no noticeable defects were observed in the micrographs of the fractured samples other than the variation in the dimple size. The tensile specimens showed an inverse relationship between strength and the dimple size of the fractured surface.

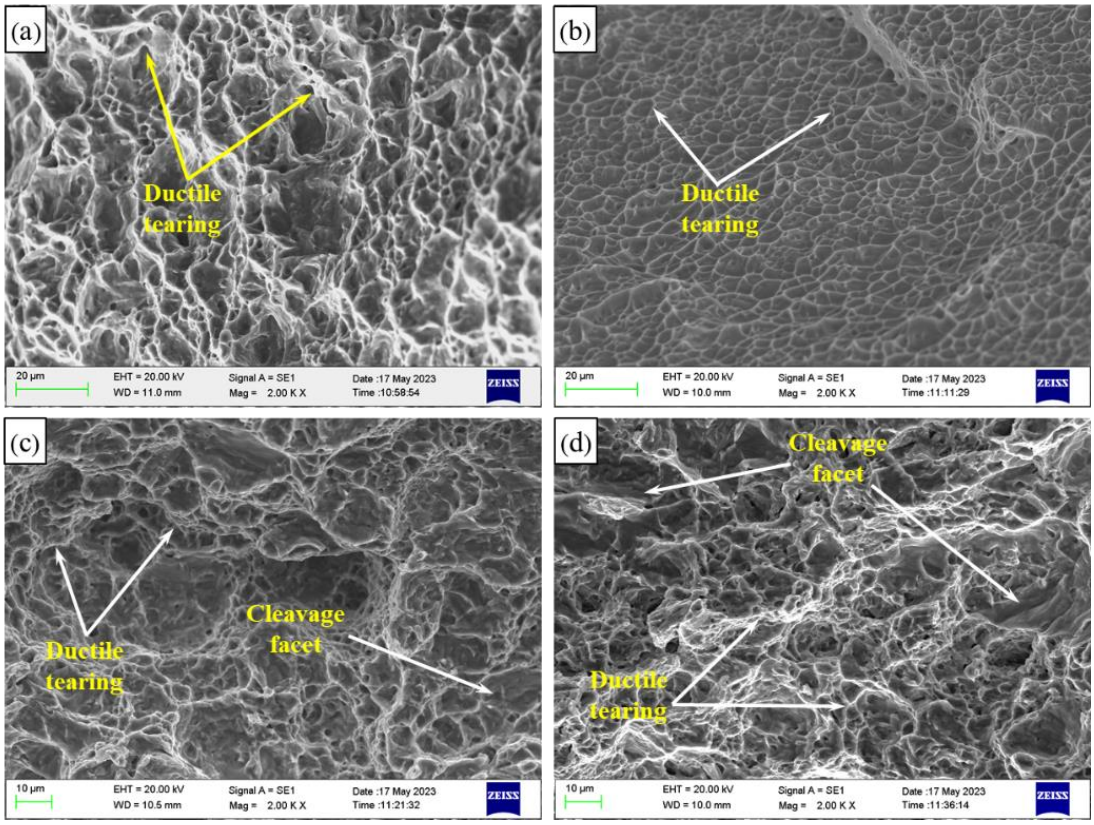

Figure 4.30 SEM micrographs of fractured reduce-section tensile specimens of as-received materials and dissimilar weld: (a) as-received CP-Ti; (b) as-received Ti-6Al-4V; (c) welded using conventional-GTAW; (d) welded using pulse-GTAW at 5Hz

Full-length tensile testing

Full-length tensile specimens were prepared to determine the weakest region and the strength of the weldment. Figure 4.31 (a) shows the polished standard (full-length) tensile specimens. These specimens were extracted from the as-received CP-Ti and Ti-6Al-4V alloys, as well as dissimilar welded samples using conventional-GTAW and pulsed-GTAW at a 5 Hz frequency. Three specimens were tested under each condition for repeatability of results at room temperature and the same strain rate, and the tested specimens followed the same trend. Figure 4.31 (b) shows the specimen mounted on the universal testing machine (UTM), and Figure 4.31 (c) shows the tested or fractured full-length tensile specimens. All tensile testing specimens fractured from the gauge section, with base material specimens fracturing

near the middle of the gauge section. However, the dissimilar weld specimens prepared using conventional-GTAW fractured away from the weld near the HAZ/base boundary towards the CP-Ti side, whereas specimens prepared from pulsed-GTAW welds fractured away from the weld near the fusion/HAZ boundary towards the CP-Ti side. During dissimilar welding of titanium alloys, tensile samples fractured away from the weld towards the weaker side of the base material [111]. The point of fracture is highlighted in Figure 4.30, shifted from the HAZ/base boundary for conventional-GTAW welds to the fusion/HAZ boundary for pulsed-GTAW. The current pulsing during GTAW changed the weakest region of the weld and also altered the strength of the weakest region. The stress-strain relationship for the full-length standard tensile specimens of the base material and welded specimens is shown in Figure 4.31 (d). All the specimens showed sufficient necking before fracture, except for the as-received Ti-6Al-4V alloy, which showed very little and localized necking. The necking phenomenon in fractured specimens reveals that the tensile specimen has failed due to ductile fracture [116]. Base CP-Ti and Ti-6Al-4V specimens showed uniform elongation across the gauge length; however, welded specimens showed non-uniform and localized elongation away from the weld in the HAZ of the CP-Ti side. The tensile specimens of welded sheets and the base of Ti-6Al-4V fractured with less total elongation in the gauge length than the base of CP-Ti specimens. All the welded specimens fractured away from the welded region, implying that the welded region is not the weakest region of the weldment. The hardness results also displayed higher hardness in the dissimilar weld region than the base and HAZ of CP-Ti.

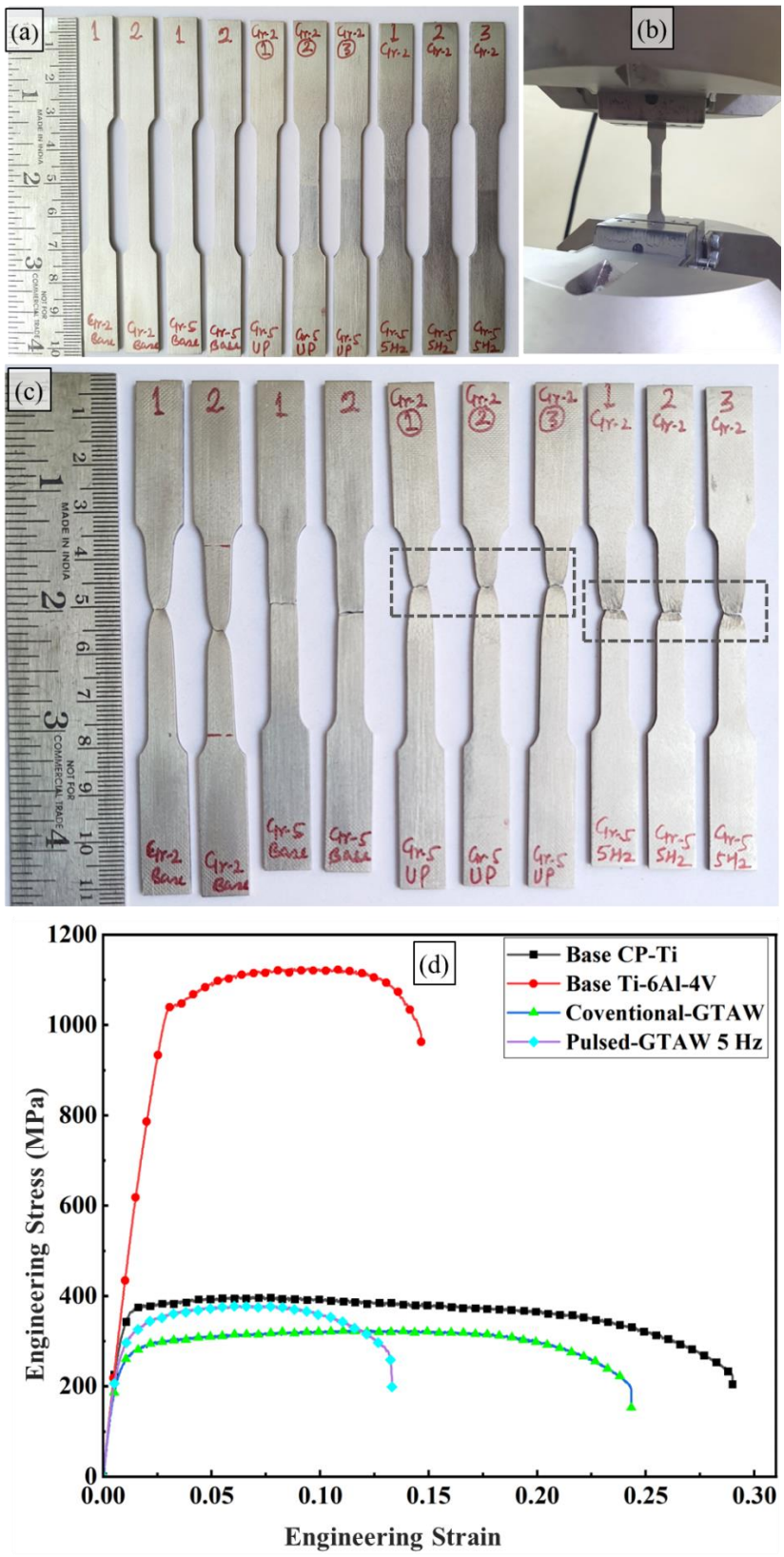

Figure 4.31 (a) Full-length tensile test specimens; (b) specimen mounted on UTM; (c) fractured full-length tensile specimens; (d) stress-strain diagram for full-length tensile test specimen

The yield strength at 0.2% offset, ultimate tensile strength (UTS), and percentage of

elongation at fracture obtained for the full-length tensile specimens are listed in Table 4.5. Similar to reduced-section tensile specimens, the base material of Ti-6Al-4V stood strongest among all the specimens, showing maximum yield strength (1043 MPa) and UTS (1123 MPa), while conventional-GTAW welded dissimilar welds showed the minimum yield strength (254 MPa) and UTS (323 MPa). Pulse-GTAW welded dissimilar welds exhibited intermediate yield strength (300 MPa) and UTS (376 MPa) but minimum percentage elongation (13.2%). Due to grain coarsening in the HAZ of the CP-Ti side, both welds fractured from the HAZ of CP-Ti, resulting in a drop in yield strength and UTS observed in the dissimilar welded specimens compared to the yield strength (364 MPa) and UTS (364 MPa) of the as-received CP-Ti. Higher strength and reduced elongation were obtained for the weld produced using pulsed-GTAW than conventional-GTAW weld. The hardness results also displayed higher hardness in the HAZ of the weld produced using pulsed-GTAW. This increase in hardness and strength in the HAZ of the CP-Ti side is attributed to the appearance of a finer microstructure (refer to Figure 4.20). The increase in yield strength and UTS and decrease in elongation using pulsed-GTAW at a 5 Hz frequency can be attributed to the formation of fine acicular α and a small amount of martensite (α') due to the low heat input and high cooling rate during pulsed-GTAW [23, 29].

Table 4.6 Results obtained from reduced-section specimens of dissimilar weld

Specimen	Yield stress (At 0.2 % offset) [MPa]	Ultimate Tensile Strength (UTS) [MPa]	% Elongation at fracture
Ti-6Al-4V (as-received)	1043	1123	14.7
CP-Ti (as-received)	364	395	29
Using Conventional-GTAW	254	323	24.3
Pulsed-GTAW (5 Hz)	300	376	13.2

Figure 4.32 (a-d) shows the SEM micrographs of the fractured full-length tensile

specimens of as-received CP-Ti, as-received Ti-6Al-4V, and dissimilar welds produced using conventional-GTAW and pulsed-GTAW at 5 Hz, respectively. When these fractured specimens were analyzed under high-resolution SEM, mostly intergranular fractures were observed, and the fractured surfaces appeared dull in all the specimens. Similar to reduced-section tensile specimens, as-received CP-Ti and Ti-6Al-4V had almost equiaxed dimples; however, finer dimples were observed in the as-received Ti-6Al-4V. Both the as-received materials were fractured in a ductile fashion, and ductile tears were clearly visible in the micrographs. The dimples observed in the fractured sample of conventional-GTAW welds were coarser and shallower than the dimples observed in the pulsed-GTAW. This was also evident from the microstructure of pulsed-GTAW welds at 5 Hz, where grain refinement took place in pulsed-GTAW in comparison to conventional-GTAW. Welded specimens had variation in dimple size in the fractured region, and more facets were observed in pulsed-GTAW welds compared to conventional-GTAW. These cleavage facets in the weld region appeared due to the formation of acicular α and a small amount of martensite (α') in the HAZ of the CP-Ti side. The number of facets and strength increased for the pulsed-GTAW welds compared to conventional-GTAW because the low heat input and fast cooling rate in pulsed-GTAW aided in the formation of more martensite and a finer microstructure in the weldment. Even though the point of fracture in pulse-GTAW shifted towards the far-HAZ of CP-Ti, refinement due to current pulsing produced finer dimples on the fracture surface. The tensile specimens exhibited an inverse relationship between strength and the dimple size of the fractured surface.

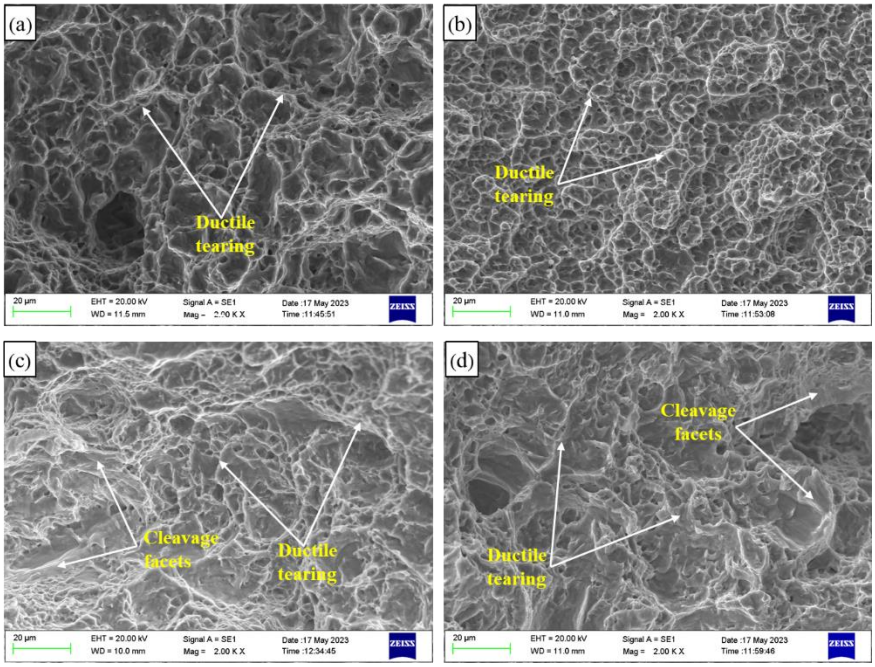

Figure 4.32 SEM micrographs of fractured full length tensile specimens of as-received base materials and dissimilar welds: (a) as-received CP-Ti; (b) as-received Ti-6Al-4V; (c) welded using conventional-GTAW; (d) welded using pulse-GTAW at 5Hz

4.4.7.3 Charpy impact testing dissimilar weld

Initially, Charpy impact testing was performed by creating a notch at the center of dissimilar welds produced using conventional-GTAW and pulsed-GTAW, at pulse frequencies ranging from 3 Hz to 5 Hz with an interval of 0.5 Hz, and base materials. Figure 4.33 (a) shows the polished Charpy impact testing specimens of base and dissimilar welds at different frequencies with a notch at the center of the weld, and Figure 4.33 (b) shows the Charpy impact tested base and dissimilar welds, where base specimens were fractured into two halves but welded specimens remained intact after testing. In welded specimens, the crack was flown inside the weld region towards the CP-Ti side.

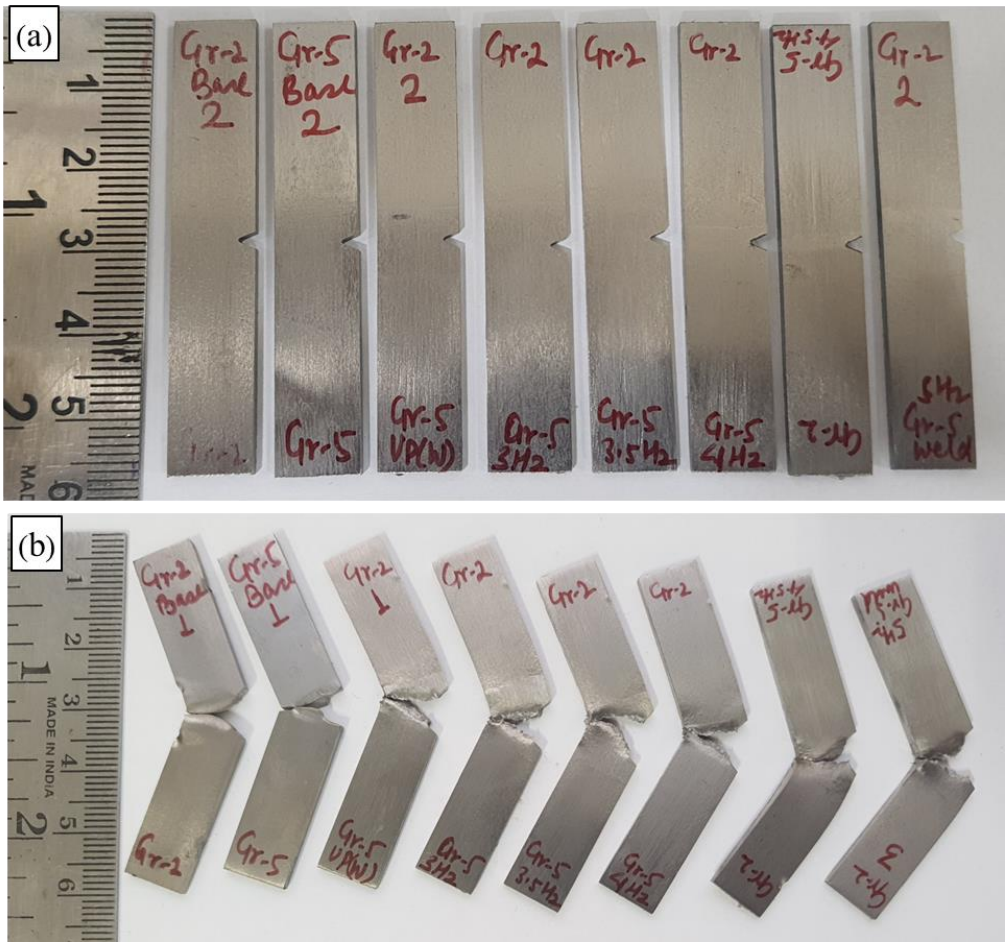

Figure 4.33 (a) Charpy impact test specimens of base and dissimilar welds at different frequency with notch at the center of the weld; (b) tested and broken specimens of base and dissimilar weld at different frequency with a notch at the center

The absorbed impact energy during the test did not exceed 80% of the rated energy of the hammer in any case. Among all the tested specimens, as-received CP-Ti absorbed the highest impact energy (200.9 J/cm^2), while as-received Ti-6Al-4V absorbed the minimum impact energy (17.7 J/cm^2). However, the impact energy absorbed for the weld region of the dissimilar weld ranged from 103.3 J/cm^2 to 88 J/cm^2. There was no considerable variation in the values of the impact energy for pulse frequencies ranging from 3 to 4 Hz; however, a considerably low value of impact energy (95.3 J/cm^2) was obtained for a 5 Hz frequency compared to the impact energy (100.3 J/cm^2) absorbed for conventional-GTAW welds. The average impact energy absorbed for the base and welded regions of dissimilar welds at

different welding conditions has been listed in Table 4.6. The decrease in impact energy with increasing pulse frequency during pulsed-GTAW can be attributed to the higher hardness in the weld region, resulting from the formation of acicular α and martensite (α') in pulsed-GTAW welds operating at high frequencies.

Table 4.7 Results of impact testing of base and weld region of dissimilar welds (at 24 °C)

Sample Name	**Avg. Impact Strength (J/cm^2)**
Ti-6Al-4V (as-received)	17.7
CP-Ti (as-received)	200.9
Using Conventional-GTAW **(weld)**	103.3
Pulsed-GTAW (3 Hz) **(weld)**	100.3
Pulsed-GTAW (3.5 Hz) **(weld)**	100.1
Pulsed-GTAW (4 Hz) **(weld)**	100.2
Pulsed-GTAW (4.5 Hz) **(weld)**	99.8
Pulsed-GTAW (5 Hz) **(weld)**	95.3

The change in pulse frequency during pulsed-GTAW of dissimilar welds did not have much effect on the energy; however, a considerable effect of current pulsing at 5 Hz was observed when compared with conventional-GTAW. Therefore, a detailed examination of the Charpy impact test was carried out on conventional-GTAW welds and pulsed-GTAW at 5 Hz. Charpy impact testing was performed to determine the impact energy of the HAZ of the CP-Ti side, the HAZ of the Ti-6Al-4V side, and the dissimilar weld region of welds prepared using conventional-GTAW and pulsed-GTAW at 5 Hz frequency. Figure 4.33 (a) shows the polished Charpy impact testing specimens of base and dissimilar welds prepared using conventional-GTAW and pulsed-GTAW at 5 Hz with notches at the center of the weld and at the HAZ of the CP-Ti and Ti-6Al-4V sides. Figure 4.33 (b) shows the Charpy impact-tested specimens mentioned above, where base specimens were fractured into two halves, but welded specimens with notches at the weld or HAZ were not completely

separated after testing. The fractured surfaces for the base of CP-Ti, weld, and HAZ appeared dull; however, the fractured surface of the base of Ti-6Al-4V appeared shiny. The base of CP-Ti, weld, and HAZ specimens fractured with significant permanent deformation, whereas the base Ti-6Al-4V fractured with little permanent deformation after impact loading. This indicates that the base Ti-6Al-4V showed a relatively brittle fracture compared to the base of CP-Ti, weld, and HAZ specimens.

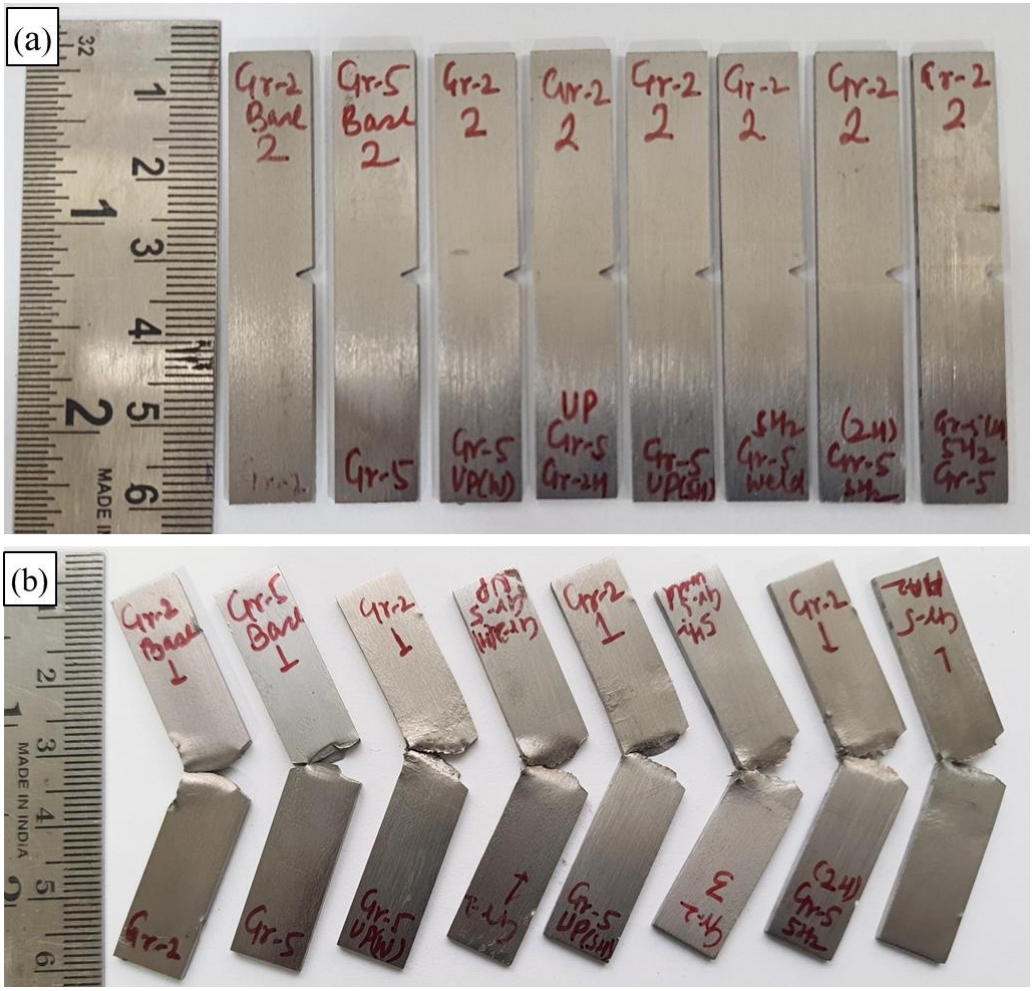

Figure 4.34 (a) Charpy impact test specimens of base and dissimilar welds with a notch at the center of the weld, and at the HAZ of CP-Ti and Ti-6Al-4V side; (b) tested and broken specimens of base and dissimilar welds with a notch at the center weld and at the HAZ of CP-Ti and Ti-6Al-4V side

The average impact energy absorbed for the base, HAZ, and weld region of dissimilar welds produced using conventional-GTAW and pulsed-GTAW at 5 Hz frequency is listed in Table 4.7. The impact energy of the HAZ of CP-Ti decreased

by 50% from the impact energy (200.9 J/cm²) of the base of CP-Ti due to grain coarsening in the HAZ of CP-Ti. The very low impact energy (17.7 J/cm²) was observed for base Ti-6Al-4V; however, the impact energy of the HAZ of Ti-6Al-4V was near the impact energy (~100 J/cm²) of the HAZ of CP-Ti. This improvement in the impact energy of the HAZ of Ti-6Al-4V was due to the appearance of Widmanstätten morphology in the HAZ of Ti-6Al-4V, which helped improve the impact energy of this region. The impact energy or toughness of the weld and both the HAZ of conventional-GTAW welds were higher than that of pulsed-GTAW welds. The decrease in impact energy using pulsed-GTAW can be attributed to the higher hardness in the HAZ and weld region, resulting from the formation of acicular α and martensite (α') in pulsed-GTAW welds at 5 Hz.

Table 4.8 Results of impact testing of base and weld region of dissimilar welds (at 24 °C)

Specimen with location of the notch	**Avg. Impact Strength (J/cm^2)**
Ti-6Al-4V (as-received)	17.7
CP-Ti (as-received)	200.9
Using Conventional-GTAW **(weld)**	103.3
Using Conventional-GTAW **(HAZ-CP-Ti side)**	100.25
Using Conventional-GTAW **(HAZ Ti-6Al-4V side)**	100.1
Pulsed-GTAW **(5 Hz weld)**	95.3
Pulsed-GTAW **(5 Hz HAZ-CP-Ti side)**	100.3
Pulsed-GTAW **(5 Hz HAZ Ti-6Al-4V side)**	93.8

Fractography of fractured surface of impact test specimens

The fractured surfaces of the impact test specimens were observed under the high-resolution scanning electron microscope (SEM). The micrographs of impact tested specimens with notch in the different regions of the weld were captured to analysed the fractured mechanism in each region. Figure 4.35 (a-b) shows the SEM

micrographs of fractured impact test specimens of as-received CP-Ti, as-received Ti-6Al-4V, Figure 4.35 (c, e, and g) shows the HAZ of CP-Ti side, weld region and HAZ of Ti-6Al-4V of conventional-GTAW weld, Figure 4.35 (d, f, and h) shows the HAZ of CP-Ti side, weld region and the HAZ of Ti-6Al-4V of pulse-GTAW weld. The as-received CP-Ti was fractured after absorbing very high impact energy and left behind tear ridges, which signifies the specimen was fractured after sufficient deformation. The as-received Ti-6Al-4V was fractured after absorbing very low impact energy, and left behind equiaxed dimples in the fractured region. It fractured with no or very low deformation and showed intergranular fracture with dimple size in the range of grain size of the as-received Ti-6Al-4V. The HAZ of the CP-Ti side of both welds was fractured in a mixed manner. Due to trans-granular fracture of large-sized prior-β grains, cleavage facets appeared, and due to intergranular fracture of small-sized grains after deformation, tear ridges appeared. Different sizes of dimples were observed in the weld region of both welds, with relatively finer dimples observed in the pulsed-GTAW weld. The fractured surface in the HAZ of the Ti-6Al-4V side of the pulsed-GTAW weld showed mostly cleavage facets due to intragranular fracture of large-sized prior-β grains. However, the fractured surface of the HAZ of the Ti-6Al-4V side of the conventional-GTAW weld showed mixed fracture patterns, with cleavage facets appearing due to intergranular fracture and tear ridges indicating deformation and energy absorption, which was higher than that of the pulsed-GTAW weld.

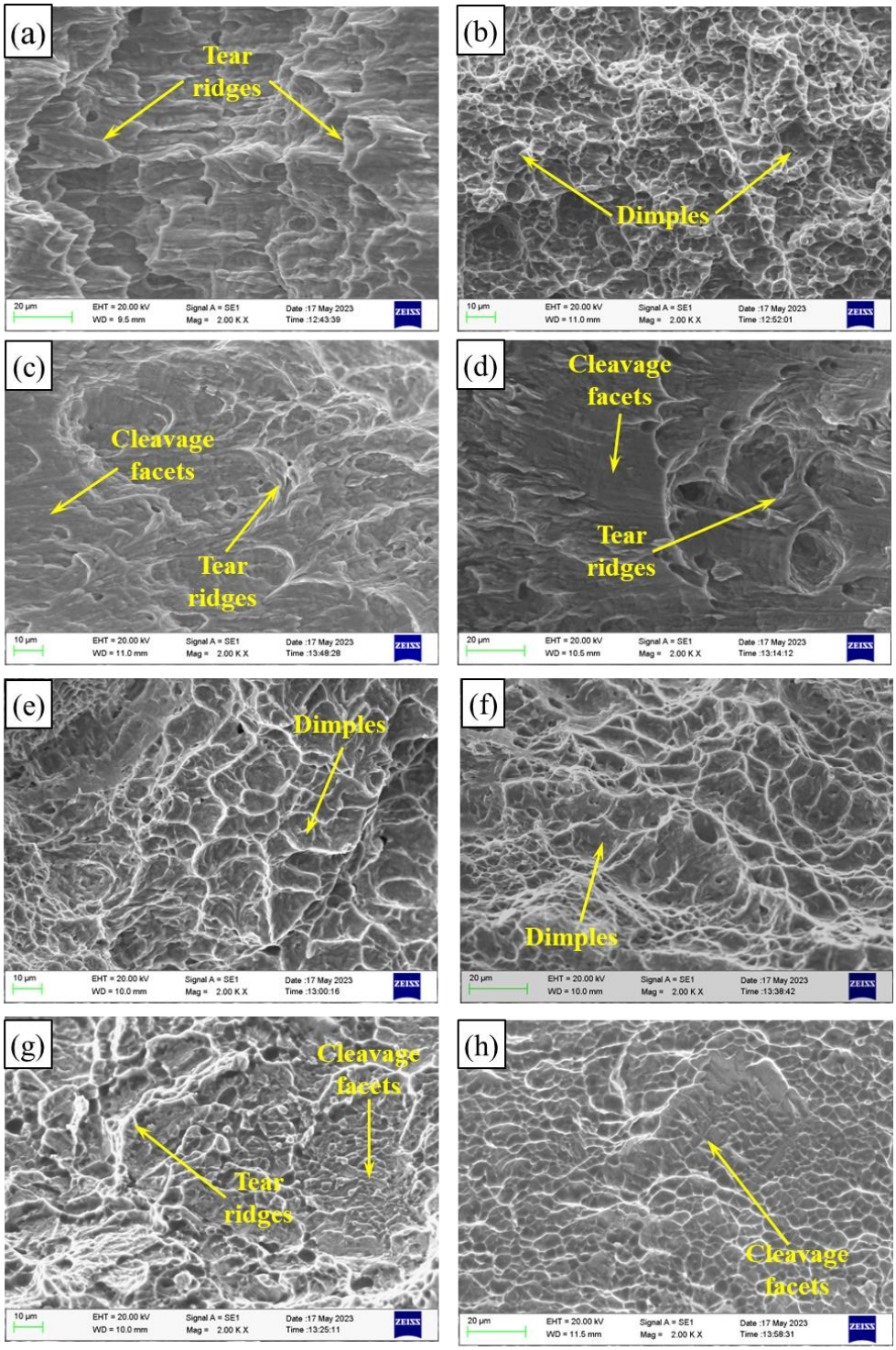

Figure 4.35 SEM micrographs of fractured impact test specimens of as-received base materials and dissimilar welds: (a) as-received CP-Ti; (b) as-received Ti-6Al-4V; (c) HAZ of CP-Ti side in conventional-GTAW weld; (d) HAZ of CP-Ti side in pulse-GTAW weld; (e) weld region in conventional-GTAW weld; (f) weld region in pulse-GTAW weld; (g) HAZ of side in conventional-GTAW weld; (d) HAZ of Ti-6Al-4V side in pulse-GTAW weld

4.4.7.4 Zone wise impression creep analysis of dissimilar weld

Samples for impression creep testing were extracted from different regions of radiographic quality pulsed-GTAW welded dissimilar titanium alloys at 5 Hz, as shown in Figures 3.14 (c, d) and 3.15 (b). The specimen size for impression creep testing was approximately 8-10 times greater than the diameter of the indenter. The extracted and impression creep-tested specimens from different regions of the weldment are shown in Figure 3.19 (c). The scheme and conditions used in terms of stress and temperature for each region for impression creep testing are discussed in Section 3.8.8 and listed in Table 3.6. For impression creep testing, five kinds of specimens were prepared from different parts of the dissimilar weld. The first specimen was extracted from the base of CP-Ti, the second from the HAZ of the CP-Ti side, the third from the dissimilar weld region, the fourth from the HAZ of the Ti-6Al-4V side, and the fifth from the base of Ti-6Al-4V. The selected stress values for impression creep testing varied from 460 MPa to 1160 MPa, ensuring that the test results are useful from an application point of view. Additionally, the tests were conducted for a sufficiently long time to obtain reliable results. The test matrix was designed to determine the stress exponent and activation energy with the minimum number of experiments. The microstructure of the impression creep-tested specimens, observed through optical microscopy, and the impression creep results are discussed in the subsequent sections.

Microscopy of impression creep tested specimens

The indentation made during impression creep testing locally deforms the material, and this deformation appears as a change in the microstructure in the deformation zone. Figure 4.36 (a) shows the dissimilar weld bead cross-section indicating different regions where impression creep testing has been performed. Figure 4.36 (b-

f) shows the optical micrographs of impression creep-tested specimens under different conditions: base of CP-Ti at 793 K and 500 MPa, HAZ of the CP-Ti side at 793 K and 500 MPa, dissimilar weld region at 848 K and 900 MPa, HAZ of the Ti-6Al-4V side at 873 K and 1110 MPa, and base of Ti-6Al-4V at 848 K and 900 MPa. In all five cases, the black region in the micrographs indicates the side view of the impression or cavity created by the indenter, and three distinct regions observed below the cavity or indent are labeled and separated using yellow curved lines. Region 1 indicates the area just below the indenter, where no significant change in the grain shape was observed. This area is also known as the ‘dead zone’, and in this region, no plastic deformation is supposed to take place. Region 2 shows the area where the indentation caused severe plastic deformation, and the grains in this area are highly deformed. Region 3 is the area far away from the indentation, and there was no evidence of plastic deformation.

The affected areas differed depending on the weldment's location. The area of the dead zone varied in each case; the widest dead zone was obtained for the base of CP-Ti, followed by the weld and HAZ of CP-Ti, and base and HAZ of Ti-6Al-4V had minimum dead zone. Along with the widest dead zone the base of CP-Ti also had the widest plastically deformed region, followed by HAZ and base of Ti-6Al-4V. However, weld zone had intermediate and HAZ of CP-Ti had narrowest plastic deformed region. A plastically deformed region appeared due to the resistance offered to deformation by the nearby region. The large-sized grains and single phase in the HAZ of CP-Ti easily accommodate deformation in a narrow region and have a minimum deformed region.

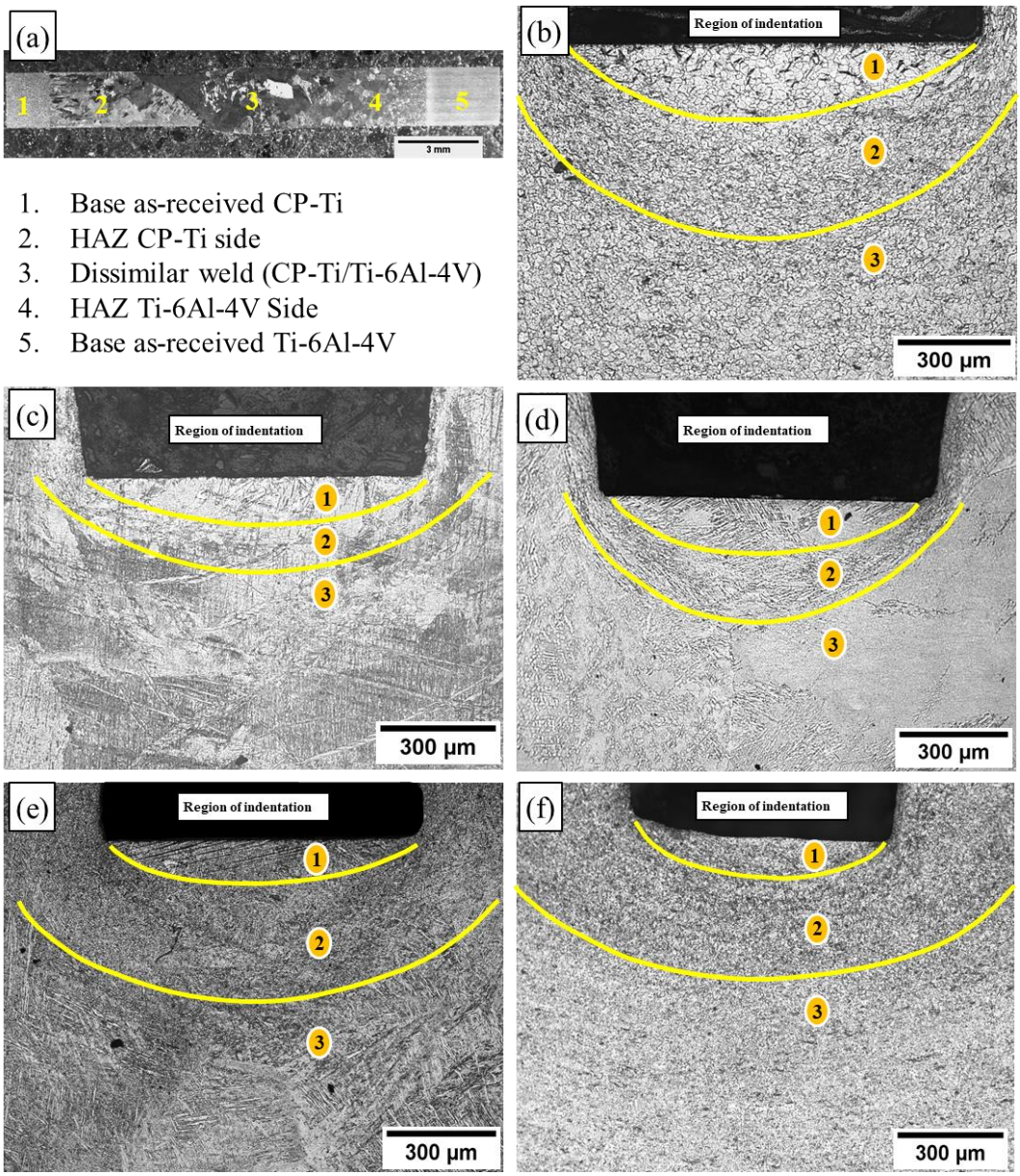

Figure 4.36 (a) Dissimilar weld bead cross-section indicating different regions; optical micrographs of impression creep tested specimens at different conditions: (b) base of CP-Ti at 793 K and 500 MPa; (c) HAZ of CP-Ti side at 793 K and 500 MPa; (d) dissimilar weld region at 848 K and 900 MPa; (e) HAZ of Ti-6Al-4V side at 873 K and 1110 MPa; (f) base of Ti-6Al-4V at 848 K and 900 MPa

Impression creep curves of different regions of dissimilar weldment

Impression creep curves were plotted to observe the secondary creep stage or creep rate-determining stage by plotting the depth of indentation with respect to time. Figure 4.37 shows the impression creep curves of different regions of the dissimilar weldment at constant temperature and variable stress. The base and HAZ of CP-Ti

were tested at 793 K and 460, 480, and 500 MPa; the dissimilar weld and base of Ti-6Al-4V were tested at 898 K and 800, 850, and 900 MPa; and the HAZ of Ti-6Al-4V was tested at 898 K and 1060, 1110, and 1160 MPa. Different regions of the weldment showed sensitivity to creep behaviour with respect to changes in stress at constant temperature. The creep rate increased with the increase in stress at constant temperature in each case; however, this effect was minimal for the base of CP-Ti, where almost the same creep rate was observed at each stress.

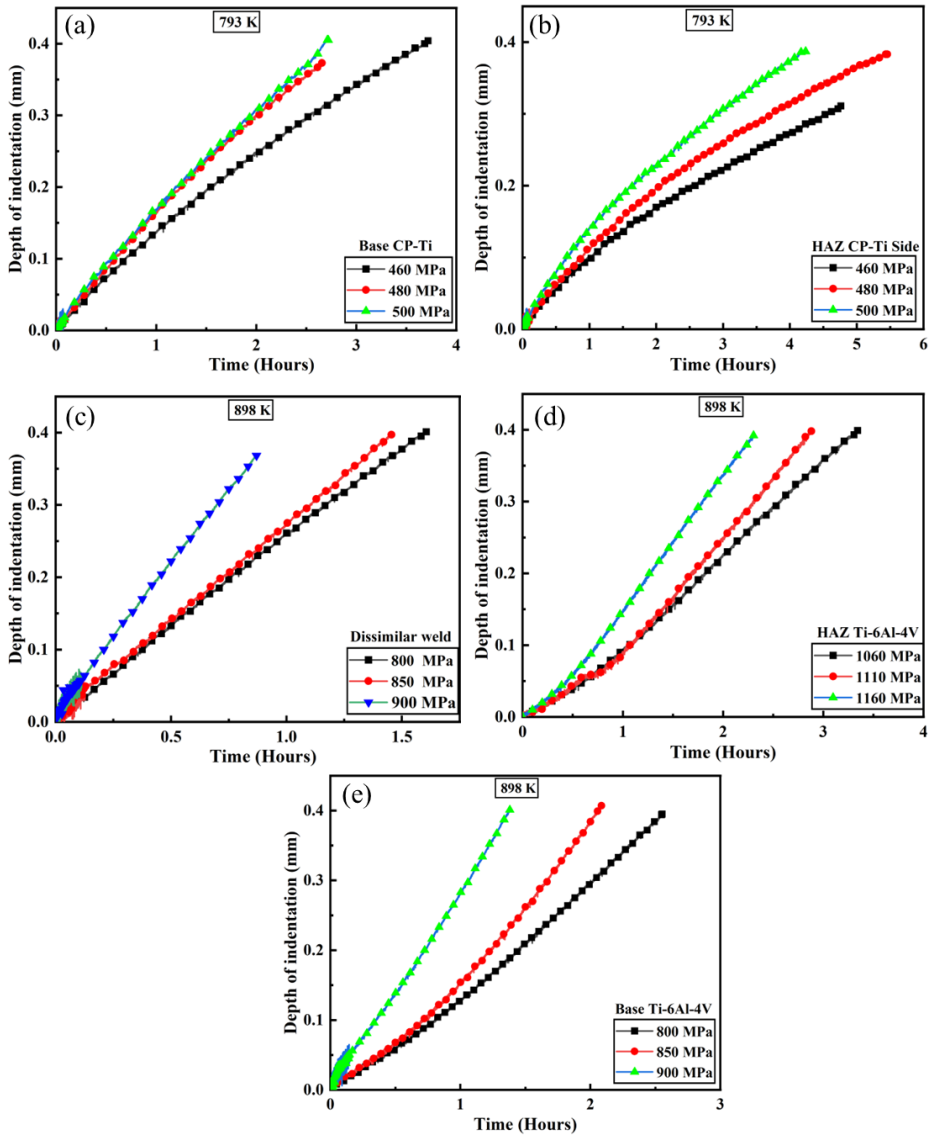

Figure 4.37 Impression creep curves of different regions of dissimilar weldment at constant temperature and variable stress: (a) and (b) at 793 K and 460, 480, and 500 MPa of base and HAZ of CP-Ti; (c) and (e) at 898 K and 800, 850 and 900 MPa of dissimilar weld and base of Ti-6Al-4V; (d) at 898 K and 1060, 1110, and 1160 MPa of HAZ of Ti-6Al-4V

Figure 4.38 shows the impression creep curves of different regions of the dissimilar weldment at constant stress and variable temperature. The base and HAZ of CP-Ti were tested at 500 MPa and 773, 793, and 813 K; the dissimilar weld and base of Ti-6Al-4V were tested at 900 MPa and 848, 873, and 898 K; and the HAZ of Ti-6Al-4V was tested at 1110 MPa and 873, 898, and 923 K. Similar to the effect of variable stresses at constant temperature, the creep rate increased with increasing temperature at constant stress in each case. All regions of the weldment, including the base region, showed very high sensitivity to temperature change at constant stress compared to the effect of stress at constant temperature. The sensitivity of temperature change on the creep rate increased with rising temperature.

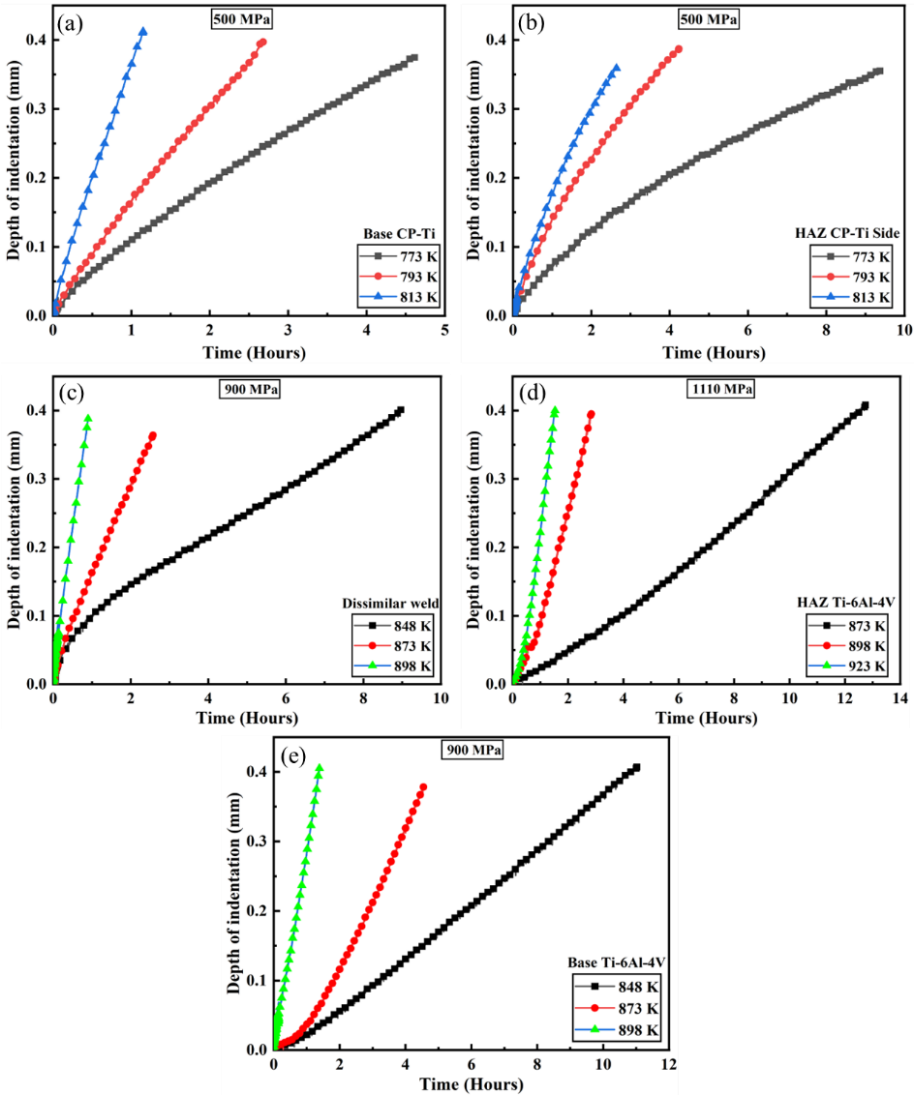

Figure 4.38 Impression creep curves of different regions of dissimilar weldment at constant stress and variable temperature: (a) and (b) at 500 MPa and 773, 793, and 813 K of base and HAZ of CP-Ti; (c) and (e) at 900 MPa and 848, 873, and 898 K of dissimilar weld and base of Ti-6Al-4V; (d) at 1110 MPa and 873, 898, and 923 K of HAZ of Ti-6Al-4V

Due to the large difference in creep strength between CP-Ti and Ti-6Al-4V alloy, all regions of the dissimilar weld cannot be tested under common conditions for comparison. The base of Ti-6Al-4V alloy has much higher creep resistance compared to the base of CP-Ti. Therefore, to compare the creep resistance of different regions of the weldment, higher stress and temperature conditions were selected for high creep strength regions. Figure 4.39 shows the impression creep curves of the base of CP-Ti, HAZ of the CP-Ti side, dissimilar weld region, HAZ of the Ti-6Al-4V side, and base of Ti-6Al-4V under different conditions. The base and

HAZ of CP-Ti were tested at 793 K and 460, 480, and 500 MPa; the dissimilar weld and base of Ti-6Al-4V were tested at 898 K and 800, 850, and 900 MPa; and the HAZ of Ti-6Al-4V was tested at 898 K and 1060, 1110, and 1160 MPa. The creep rates observed under these conditions are listed in Table 4.8. It is clear from the slopes of the impression creep curves and the creep rate data that even at higher stress and temperature values, the HAZ of Ti-6Al-4V (8.83×10^{-6} s^{-1}) showed higher creep strength due to the large grain coarsening of prior-β grains and the appearance of a Widmanstätten basket weave-type morphology in the region. The base of CP-Ti showed the highest steady-state creep rate (3.55×10^{-5} s^{-1}) at lower stress and temperature values and had the minimum creep resistance. The creep strength of the HAZ on the CP-Ti side increased compared to the base of CP-Ti due to grain coarsening in the HAZ. The steady-state creep rate of the dissimilar weld region and the base of Ti-6Al-4V (9.8×10^{-6} s^{-1}) were closer under the same conditions. The improvement in the creep resistance of the dissimilar weld compared to the base of CP-Ti was observed due to the appearance of coarse prior-β grains and Widmanstätten morphology inside the grains.

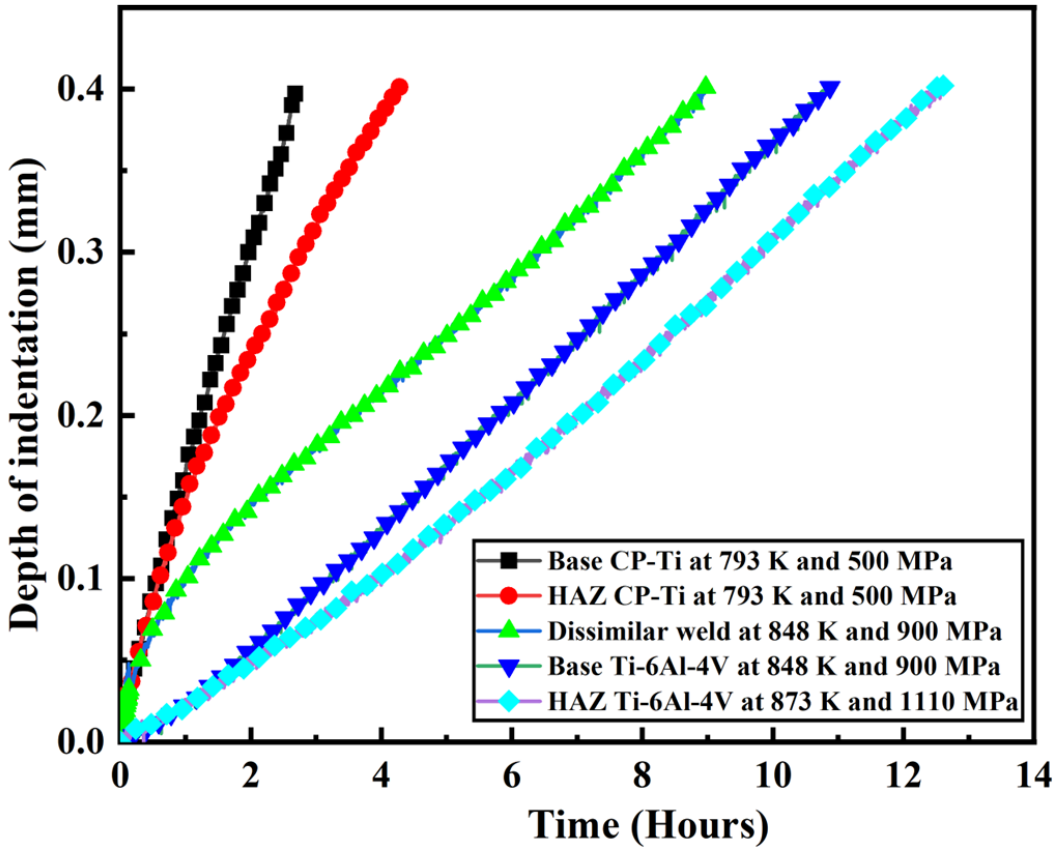

Figure 4.39 Impression creep curves of base of CP-Ti, HAZ of CP-Ti side, dissimilar weld region, HAZ of Ti-6Al-4V side, and base of Ti-6Al-4V at different condition shown in legends

Table 4.9 Steady-state creep rates (mm/s) in different regions of dissimilar weldment at different conditions

Conditions/ Location of indentation	**793 K/ 500 MPa**	**848 K/ 900 MPa**	**873 K/ 1110 MPa**
Base of CP-Ti	3.55×10^{-5}	--	--
HAZ of CP-Ti side	2.32×10^{-5}	--	--
Dissimilar weld	--	1.01×10^{-5}	--
Base of Ti-6Al-4V	--	9.8×10^{-6}	--
HAZ of Ti-6Al-4V side	--	--	8.83×10^{-6}

The effect of microstructural and sub-structural features, along with composition variation in the different zones of the weldment, contributed to the different creep behaviours observed in these zones. New microstructural and sub-structural features appeared after the impression creep test in respective zones due to dynamic

restoration. To gain further insights, activation energy and stress exponent were obtained in each zone from the steady-state region of the impression creep tests. For example, Figure 4.40 shows the semi-log plot of creep rate versus time for the base metal at a stress of 900 MPa and a temperature of 848 K. The horizontal portion of the plot indicates the steady-state region of the impression creep test. The steady-state creep rates for all five regions at different testing conditions were determined. The activation energies from the impression creep data were obtained using a method similar to that used for the conventional creep method, as stated in Equation (3.6).

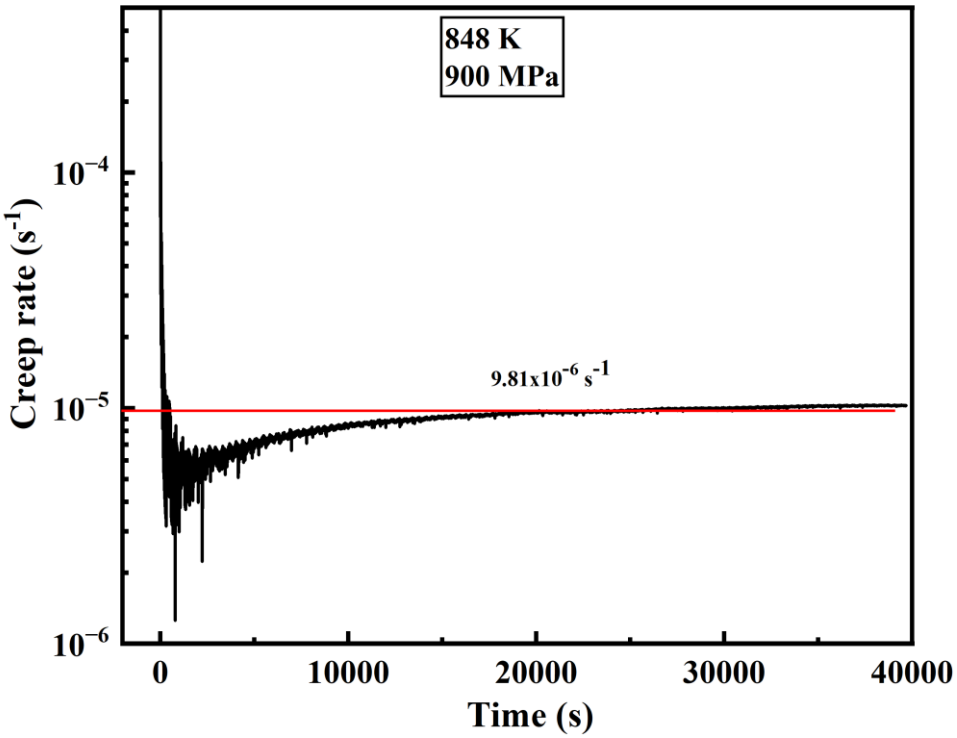

Figure 4.40 Semi-log plot between creep rate versus time for base of Ti-Al-4V at 900 MPa and 894 K

Using Equation (3.6), semi-log plots between steady-state impression velocities (or creep rate) and the inverse of testing temperatures on an absolute scale were plotted for all the regions of the weldment to determine the activation energy in each case. For example, Figure 4.41 shows the semi-log plot for the base of Ti-6Al-4V at 900 MPa at different testing temperatures. The plot represents the dependence of steady-

state creep rate on temperature at constant stress. The activation energy for the base metal was estimated by equating the slope of the straight line to Qc/2.3R. The activation energy of the base metal was calculated to be 255 kJ/mol. Similarly, the values of activation energies for other regions of the weldment were evaluated and listed in Table 4.9. The activation energies obtained from the impression creep test of different regions of the weldment ranged from 134 to 312 kJ/mol. This range of activation energy fits quite well with titanium self-diffusion values, confirming the role of dislocation climb during creep [130]. These creep activation energies were consistent with those reported from conventional creep tests for (α+β) and α titanium alloys [131].

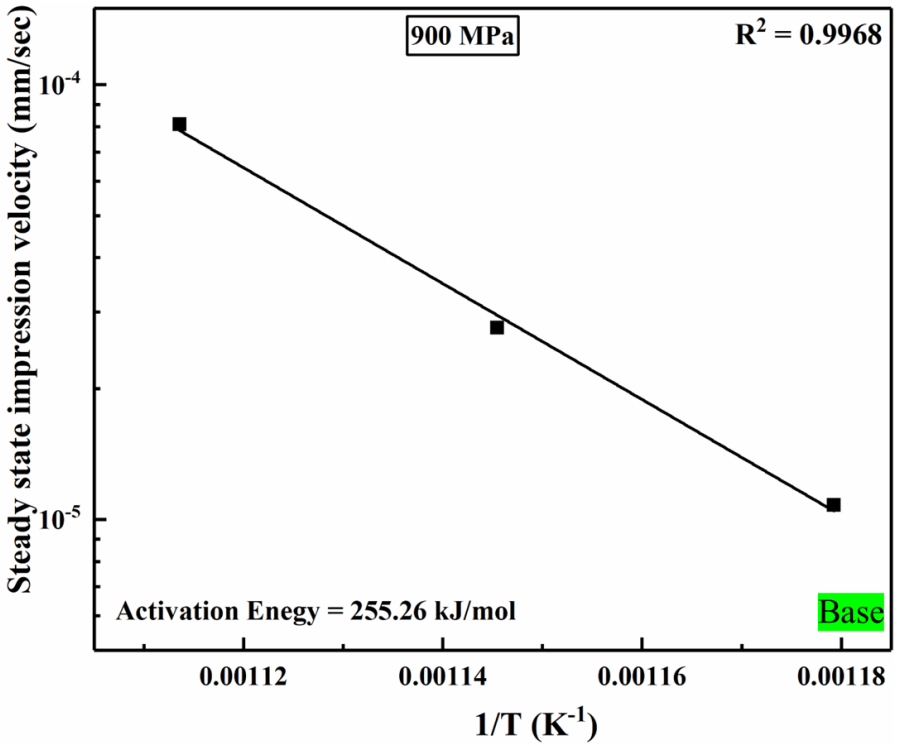

Figure 4.41 Semi-log plot between the steady-state impression velocity and the inverse of testing temperatures for base metal of Ti-6Al-4V

Table 4.10 Activation energy and stress exponent of different regions of the weldment

Location of Indentation	Activation Energy (kJ/mol)	Stress exponent (n)
Base (CP-Ti)	134.56	5.68
HAZ (CP-Ti)	171.10	4.26
Dissimilar Weld (CP-Ti/ Ti-6Al-4V)	180.52	4.62
HAZ (Ti-6Al-4V)	302	3.77
Base (Ti-6Al-4V)	255	4.45

Furthermore, in order to determine the dominant mechanism for creep deformation, the value of the stress exponent 'n' was determined using the range of stresses at constant temperature. For example, a semi-log plot between steady-state impression creep velocities and punching stresses was plotted for base metal at 898 K, as shown in Figure 4.42.

The value of the stress exponent 'n' was evaluated using the slope of the straight line from the plot, and it was found to be 4.45 for the base metal of Ti-6Al-4V. The values of the stress exponent ranged between 3 and 5 in all the regions of the weldment. The stress exponent values obtained from impression creep testing were consistent with those obtained for titanium alloys using conventional creep methods [132, 133]. The range of the stress exponent indicates that creep deformation in these regions occurred via dislocation creep [134]. The activation energy and stress exponent ranges suggest that dislocation glide and lattice diffusion-controlled dislocation climb motions contribute to deformation [135].

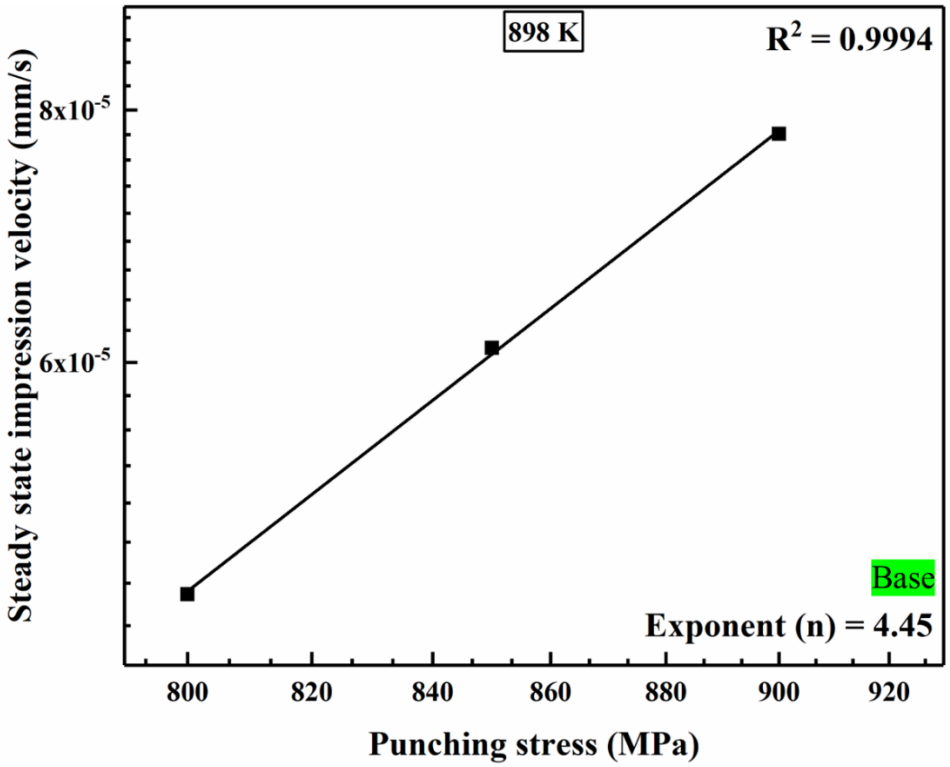

Figure 4.42 Semi-log plot of steady-state impression creep velocity versus punching stress at 898 K for base Ti-6Al-4V

After analyzing the impression creep test results, it was observed that the dissimilar weldment produced using the pulse-GTAW process had the highest creep resistance in the HAZ of Ti-6Al-4V, and the dissimilar weld region had creep resistance close to that of the base of Ti-6Al-4V. The base of CP-Ti had the minimum creep resistance in all the regions of the weldment, acting as the weakest link in the weldment at elevated temperatures. The pulse-GTAW process may be a good choice for welding dissimilar titanium alloy components for high-temperature applications. However, it is recommended to modify the microstructure of base CP-Ti from equiaxed to coarse prior-β with acicular morphology prior to welding for improved creep life of the weldment. The Widmanstätten morphology in Ti-6Al-4V could be obtained through the heat treatment route, where the base of CP-Ti needs to be heated above the β-transus temperature (~883°C) and air-cooled to room temperature.